SANDIA REPORT
SAND2007-0375
Unlimited Release
Printed January 2007

Experiments for calibration and validation of plasticity and failure material modeling: 304L stainless steel

Sam X. McFadden, Ken L. Lee, John S. Korellis

Prepared by
Sandia National Laboratories
Albuquerque, New Mexico 87185 and Livermore, California 94550

Sandia is a multiprogram laboratory operated by Sandia Corporation,
a Lockheed Martin Company, for the United States Department of Energy's
National Nuclear Security Administration under Contract DE-AC04-94AL85000.

Sandia National Laboratories

Issued by Sandia National Laboratories, operated for the United States Department of Energy by Sandia Corporation.

Available to DOE and DOE contractors from

U.S. Department of Energy
Office of Scientific and Technical Information
P.O. Box 62
Oak Ridge, TN 37831

Telephone: (865) 576-8401
Facsimile: (865) 576-5728
E-Mail: reports@adonis.osti.gov
Online ordering: http://www.osti.gov/bridge

Available to the public from

U.S. Department of Commerce
National Technical Information Service
5285 Port Royal Rd.
Springfield, VA 22161

Telephone: (800) 553-6847
Facsimile: (703) 605-6900
E-Mail: orders@ntis.fedworld.gov
Online order: http://www.ntis.gov/help/ordermethods.asp?loc=7-4-0#online

SAND2007-0375
Unlimited Release
Printed January 2007

Experiments for calibration and validation of plasticity and failure material modeling: 304L stainless steel

Sam X. McFadden, Ken L. Lee, John S. Korellis

Sandia National Laboratories
P. O. Box 969
Livermore, California 94551-0969

Abstract

Experimental data for material plasticity and failure model calibration and validation were obtained from 304L stainless steel. Model calibration data were taken from smooth tension, notched tension, and compression tests. Model validation data were provided from experiments using thin-walled tube specimens subjected to path dependent combinations of internal pressure, extension, and torsion.

Acknowledgements

Mike Chiesa performed preliminary validation test simulations and provided a validation test matrix containing path dependent combinations of pressure, rotation, and axial displacement. Sangwok (Simon) Lee assisted with the validation experiments. This work was supported by Campaign 6.

Contents

Tables

Figures

This page intentionally left blank.

1. Introduction

This work was conducted to provide the experimental basis for calibration and validation of metal plasticity and failure models. The stainless steel alloy 304L was selected as a structural material of general interest to Sandia. Although 304L has been extensively characterized, ongoing model application and development efforts require complete stress-strain or load-displacement histories from a range of specimen geometries and test conditions. Such data is not generally available. Therefore, significant laboratory work is required to provide the necessary basis for modeling plasticity and failure, even for common alloys such as 304L. Much of the data presented here have been entered into the Materials Weapon Information System and Data Management application (WISDM) [1].

Certified WR raw stock was purchased from Allied Signal Aerospace (KCP) in the form of 4 in diameter bar. Material certification is included in Appendix A. All specimens used for this study were extracted from the same lot of material. Constitutive model calibration data were obtained from smooth tension, notched tension, and compression tests. Not all material models in use at Sandia require each of these specimen geometries for calibration. However, if a specimen geometry is not needed for calibration the data may be used to verify calibration or as first-level validation. Validation data were obtained using thin-walled tube specimens subjected to complex stress and strain states through the application of internal pressure combined with axial and torsional loading. The specimen geometry and loading conditions did not support principal stresses or strains normal to the specimen surface. Consequently, the stress and strain states covered a range of bi-axial conditions. Because each of the three actuators (axial, torsional, and pressure) were operated under closed-loop control, it was possible to explore the path dependence of plasticity and failure over a wide range of loading conditions.

This page intentionally left blank.

2. Experimental details

2.1. Calibration tests

Tensile specimens were extracted from .50 in, 1.10 in, and 1.60 in radius circles with respect to the center of the 4 in diameter rod, oriented with the tensile axis parallel to the extrusion direction. The nominal dimensions of tensile specimens used in this work are listed in Table 1. The notched tension specimen design has been used extensively for investigation of the damage parameters that are part of the BCJ and EMMI material models. All tension tests were conducted under actuator stroke control of .002 in/s, which resulted in a measured true strain rate of approximately .001 in/s in the smooth tension specimens. Compression specimens were extracted on 1.50 in radius circles with respect to the rod center. The specimens were .350 in diameter and .450 in long. The specimen ends were grooved, and the grooves were filled with molybdenum grease during testing. Compression tests were run under true strain rate control of .001/s. Examples of raw stock after specimen extractions are shown in Figure 1. Figure 2 shows examples of the calibration specimens.

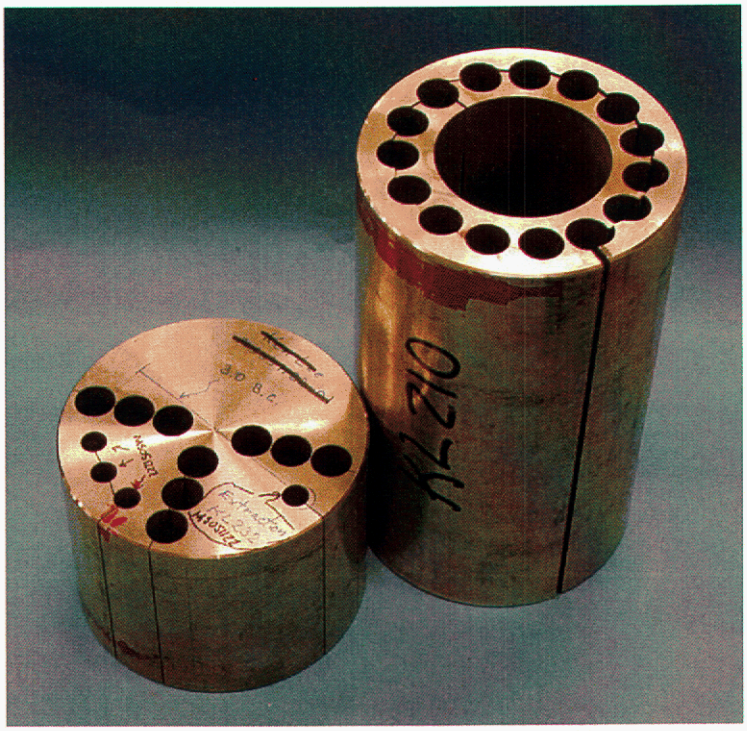

Figure 1. Examples of raw stock after specimen extraction. The large center extraction shown on the right was used in a different project.

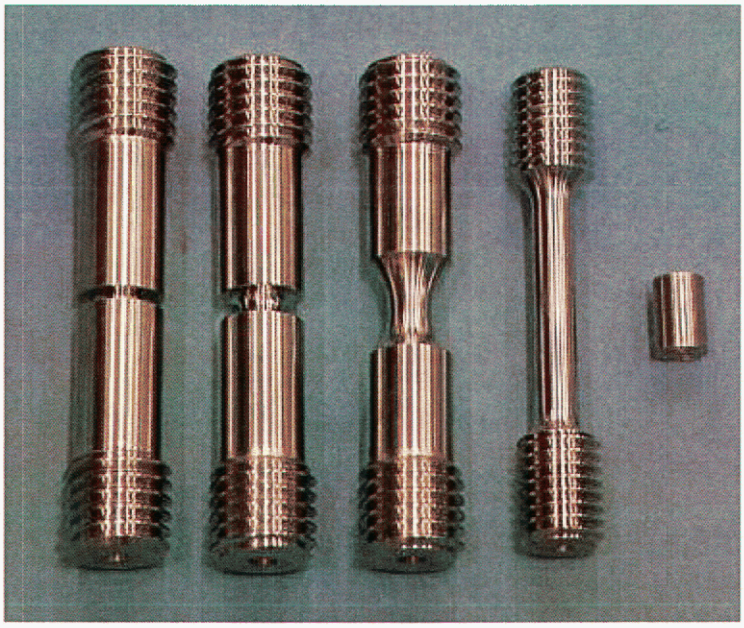

Figure 2. Calibration specimens. From left to right: notched tension (R1, R2, R4), smooth tension, and compression.

Table 1: Tensile specimen nominal dimensions.

Specimen	Gage diameter (in)	Gage length (in)	Shoulder diameter (in)	Notch radius (in)
Smooth	.250	1.00	NA	NA
Notched R1	.250	NA	.5	.039
Notched R2	.250	NA	.5	.078
Notched R4	.250	NA	.5	.390

2.2. *Validation experiments*

The model validation specimen geometry is shown in Figure 3. The specimens were extracted with centers located 1.0 in from the rod center. Measurements of the as-machined specimen inner diameters (ID) showed an average of .8755 in with a standard deviation of .0005 in. Measurements of the as-machined specimen gage section outer diameters (OD) showed and average of .9995 in, with a standard deviation of .0005 in. Each of the servo-hydraulic actuators that controlled pressure, extension, and rotation were operated under closed loop control. Here, "stroke" is used to denote actuator axial displacement, and "rotation" to denote actuator rotational displacement. To simplify the model boundary conditions that would correspond to each experiment, test frame control signals were restricted to stroke, rotation, and pressure.

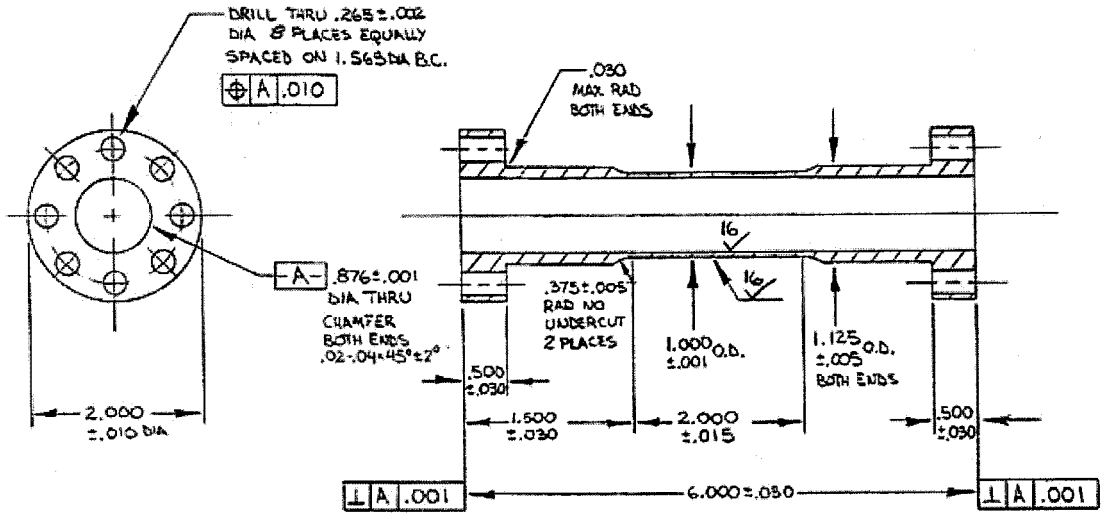

Figure 3. Validation specimen geometry.

Because the stroke and rotation data contained load frame displacements in addition to specimen displacements, the load frame compliance was measured by mounting a solid steel link in place of a validation test specimen. The steel link geometry was similar to the validation specimens, but the diameter was 1.125 in, and the length between flanges

was 2.5 in. The axial and torsional loads were independently ramped, and the stroke and rotation signals were recorded with the loads. By comparing measured stroke and rotation to calculated elastic deflection of the solid link, load frame compliance may be accounted for when comparing simulations to the experimental data.

The validation test matrix is shown in Table 2. Each step shown in the table was run sequentially, and the indicated signal was controlled with a linear ramp to the specified level. At the end of each step, the indicated signal was held constant at the specified level. For example, in load path 8, step 1, the pressure was ramped to 4000 psi while the rotation and stroke were held at 0° and 0 in. In step 2, the pressure was held constant at 4000 psi while the rotation was ramped to 30°, and the stroke was held at 0 in. In step 3, the pressure and rotation were maintained at 2500 psi and 30°, while the stroke was ramped until specimen failure. Ramp rates for pressure, rotation and stroke were 19 to 36 psi/s, .25 °/s, and .002 in/s respectively. All validation tests were conducted at laboratory temperature (70°F).

Table 2: Validation experiment matrix.

Load Path	Step1	Step 2	Step 3	Tube
1	Rotation 0°	Pressure to 8000 psi	Stroke to failure	1
2	Rotation 0°	Pressure to 4000 psi	Stroke to failure	2
3	Pressure to 4000 psi	Stroke to .10 in*	Rotation to failure**	3
4	Pressure to 4000 psi	Stroke to .20 in*	Rotation to failure**	4
5	Pressure 0 psi	Rotation to 30°	Stroke to failure	5
6	Pressure 0 psi	Rotation to 60°	Stroke to failure	6
7	Pressure 0 psi	Rotation to 85°	Stroke to failure	7
8	Pressure to 4000 psi	Rotation to 30°	Stroke to failure	8
9	Pressure to 4000 psi	Rotation to 60°	Stroke to failure	12
10	Pressure to 4000 psi	Rotation to 85°	Stroke to failure	9
11	Pressure to 8000 psi	Rotation to 30°	Stroke to failure	10
12	Pressure to 8000 psi	Rotation to 60°	Stroke to failure	11

* Step 2 was run in stroke control to the axial displacement gage signal level shown, then stroke was held constant during step 3, rotation to maximum angular displacement.
** Failure in buckling.

2.3. *Test frames and instrumentation*

All tests were completed on MTS servo-hydraulic load frames equipped with MTS TestStar Classic hardware and software. Force was measured with standard MTS load cells, and tension test displacements were measured with 1.0 in gage length MTS extensometers.

The complex loading validation tests were completed on a MTS load frame with 100 kip axial and 50 kip torsional capacity. Specimen internal pressure was provided by a MTS 286.50 pressure intensifier, which used a servo-hydraulic ram to pressurize and control water that was fed into the test specimen. Pressure was measured near the inlet port to the specimen, with a 10 ksi transducer and TestStar DC signal conditioner. The pressure control feedback signal was provided by a pressure sensor located on the water inlet line to the test fixture. Stroke and rotational control feedback signals were obtained from a LVDT and a RVDT that were integral to the load frame. Axial, diametric, and rotational displacements were measured on the specimen using the displacement gage assembly shown in Figure 4 [2]. The displacement gage employed LVDT's and RVDT's. The signals were processed with three TestStar AC conditioners. The axial displacement gage length of 1.0 in was determined by the distance between the locator pins in the assembly. Figure 8 shows the displacement gage mounted on a specimen.

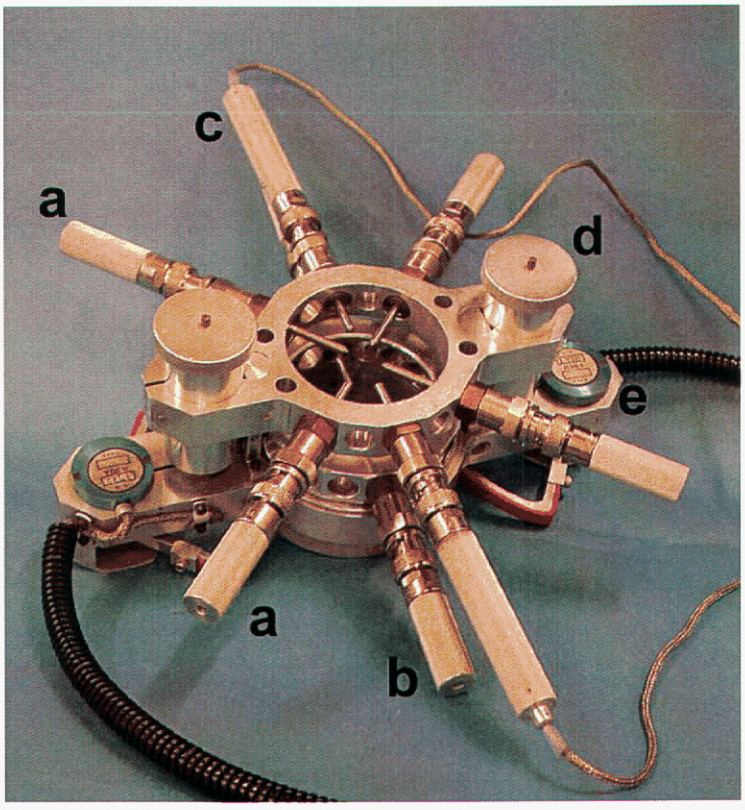

Figure 4. Axial, diametric, rotational displacement gage. The gage fits around the validation specimen. Two pairs of conical tip spring loaded contact pins (a) fix the top half of the gage to the specimen, while one pair (b) fixes the bottom half, with 1.0 in of vertical separation (gage length). Two similar opposing pins in the top half (c) contain LVDT's that measure diametric displacement. Axial displacement is obtained from two LVDT's (d) that measure the displacement between the upper and lower sets of contact pins. Rotational displacement is obtained from two RVDT's (e) that measure the angular difference between the upper and lower sets of contact pins. The signal from each pair of LVDT's and RVDT's is summed to provide an average displacement.

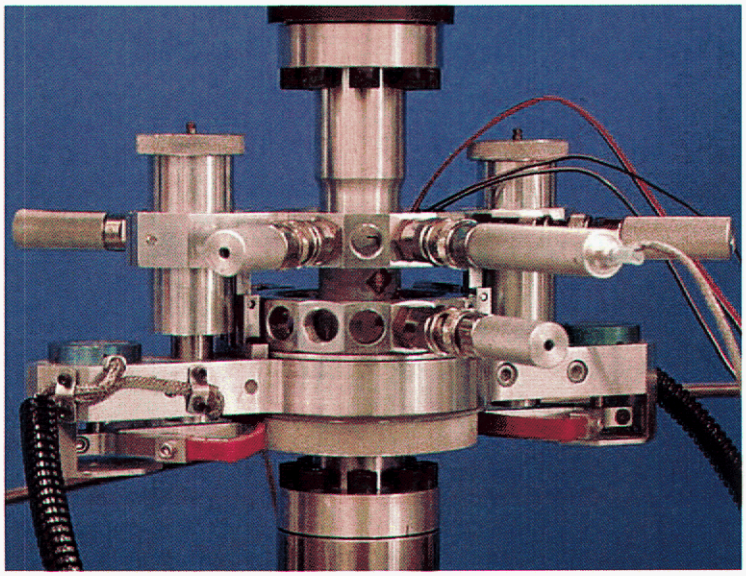

Figure 5. Validation specimen and displacement gage.

2.4. Measurement accuracy and precision

The measurement accuracy and precision of this work was established by load and displacement transducers calibrated in accordance with industry standards using measurement values traceable to the National Institute of Standards and Technology (NIST). The MTS LVDT's and RVDT, integral to the load frames, were calibrated in accordance with MTS Procedure FS-CA 2104 Rev. E. MTS load cells were calibrated in accordance with ASTM E4-03. Error for the calibrations was less than 0.25% of reading, with an uncertainty of ±0.25% for a confidence level of 95%. All sensor and signal conditioning systems not calibrated by MTS were calibrated at time of use by comparison to standards traceable to the National Institute of Standards and Technology.

3. Results

3.1. Calibration data

Smooth tension data is shown in Figure 6. No significant affect of radial position on tensile properties was observed. Figure 7 shows a plot of the measured true strain rate vs. time. Notched tension load-displacement data is shown in Figure 8. Compression stress-strain curves are shown in Figure 9. The compression specimens shown in Figure 10 demonstrate uniform deformation.

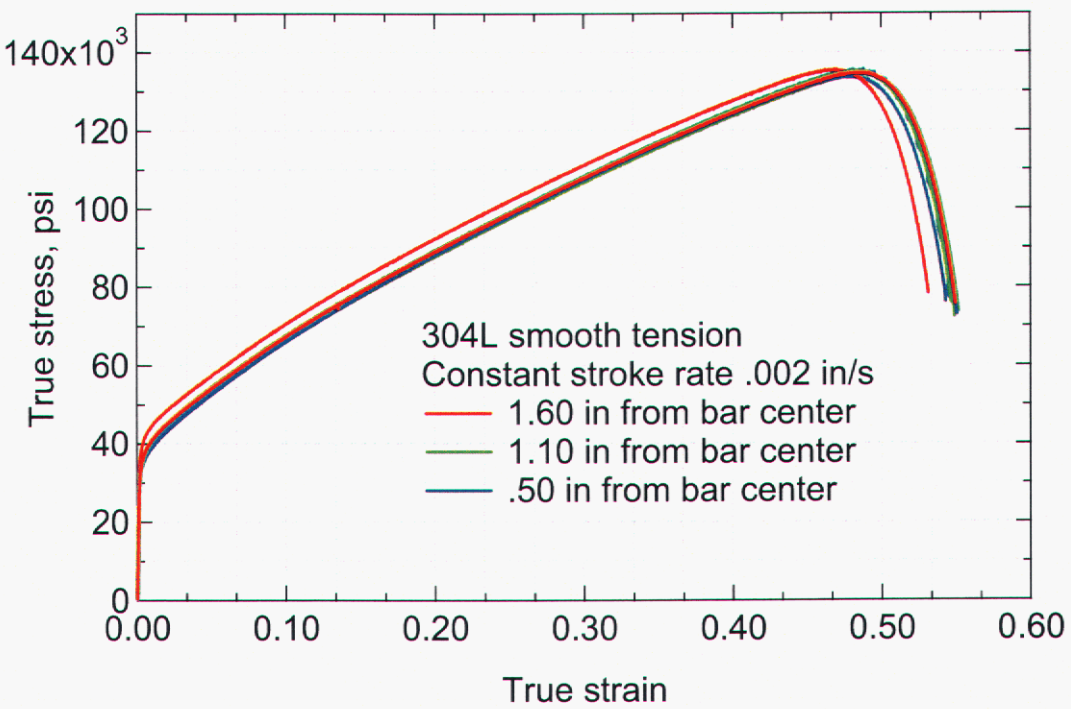

Figure 6. Smooth tension true stress vs. true strain curves. Nominal displacement rate was .002 in/s.

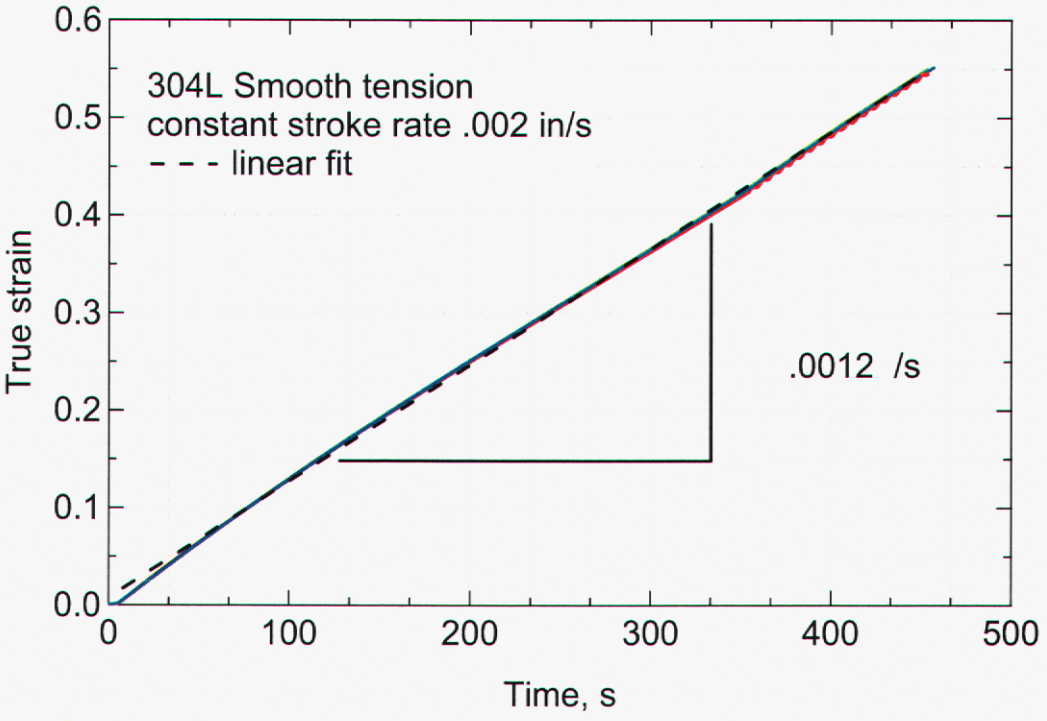

Figure 7. Measured true strain vs. time. The data is from the tests shown in Figure 6.

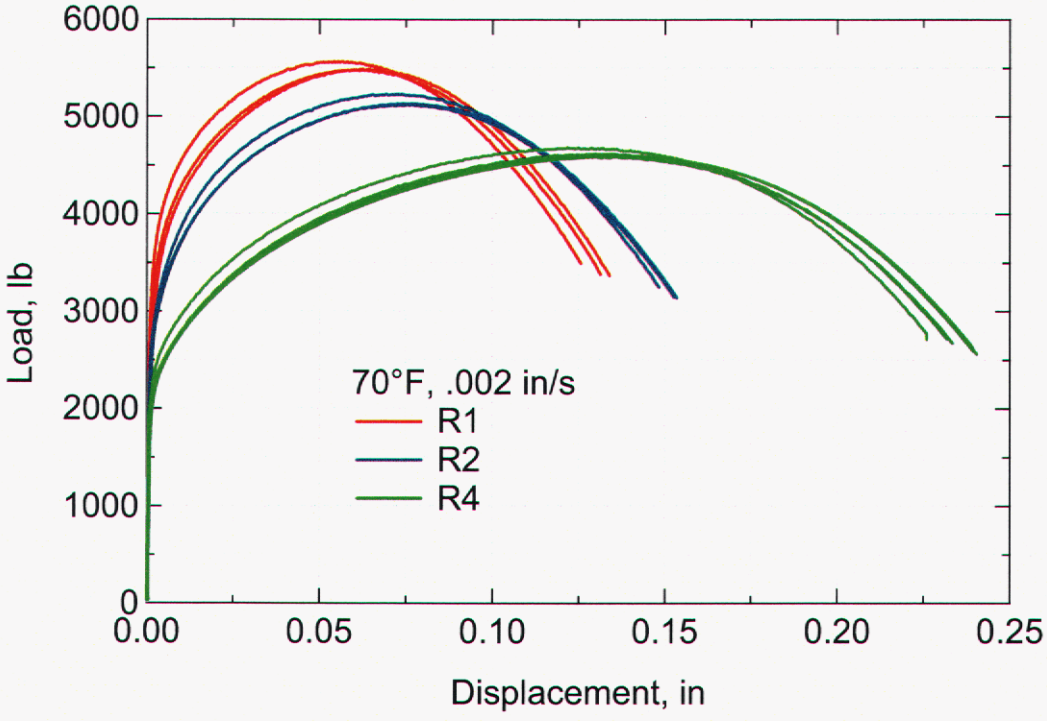

Figure 8. Notched tension load-displacement data.

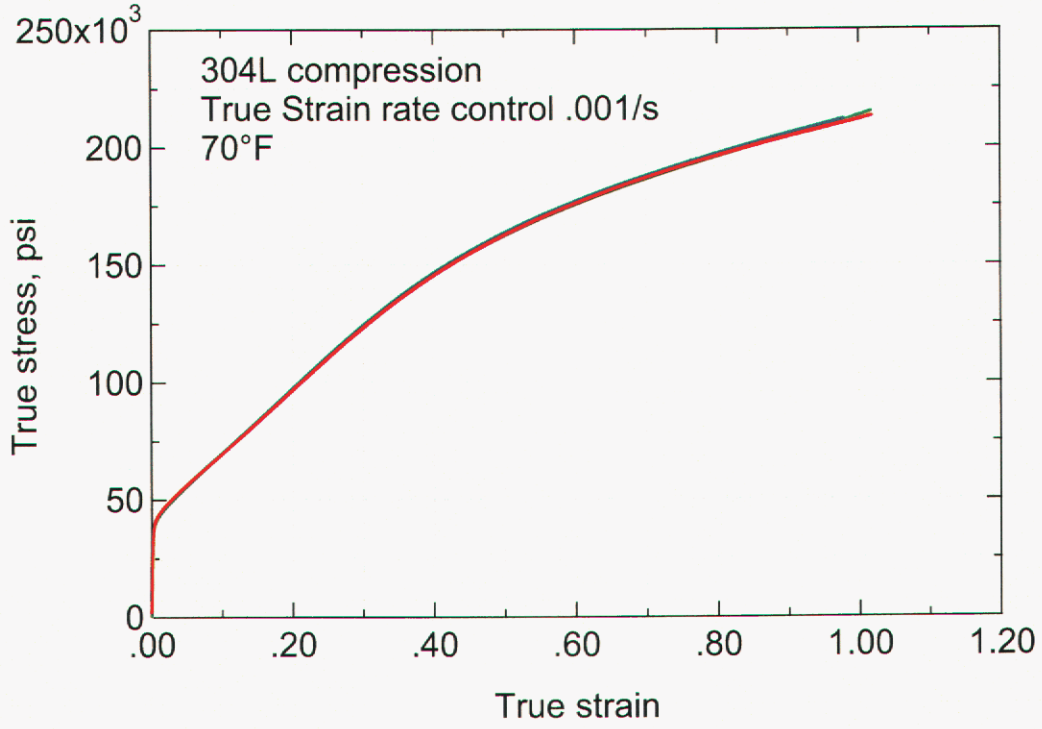

Figure 9. Compression data.

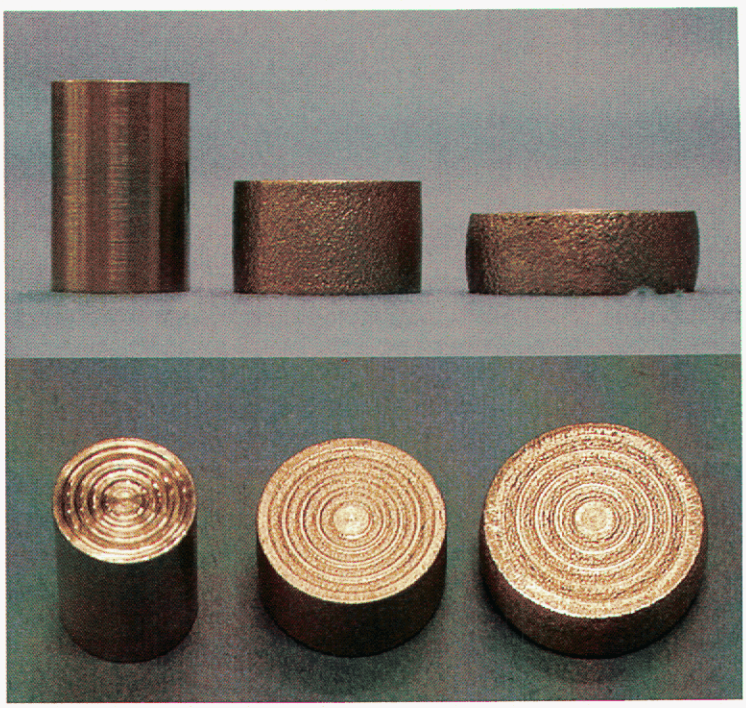

Figure 10. Compression specimens. The specimen on the left is as-machined. The specimen on the right was deformed to a true strain of 1.02.

3.2. *Validation data*

The validation test data is presented here as a function of time. Pressure is plotted with diametric displacement. Torque is plotted with rotation and angular displacement. Rotation is a measure of the hydraulic actuator angular position obtained from the load frame RVDT, and angular displacement was measured on the specimen using the displacement gage described previously. Load is plotted with stroke and axial displacement. Stroke is a measure of the hydraulic actuator axial position, and axial displacement was measured on the specimen using the displacement gage described previously. The differences between the rotation and angular displacement measurements, and between the stroke and axial displacement measurements, are mostly due to the dimensions of the displacement gage, although load frame compliance contributed a small part. The difference between rotation and angular displacement measurement is shown schematically in Figure 11.

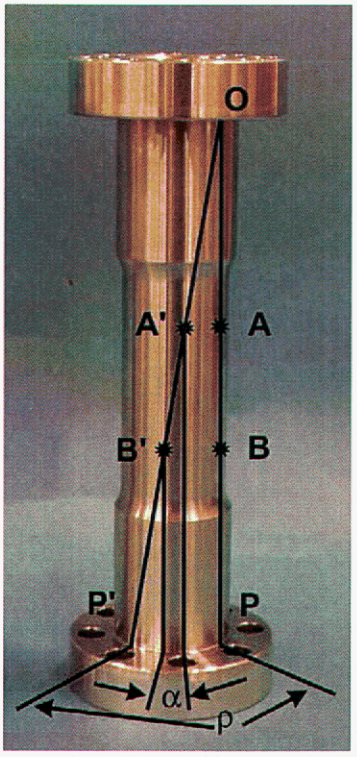

Figure 11. Schematic representation of the difference between rotation and angular displacement measurements. The line OP represents a line drawn on the specimen prior to straining in torsion. The line OP' approximates the line OP after straining. Before straining, the upper half of the displacement gage is pinned at A and the lower half is pinned at B. After straining, A is rotated to A', and B is rotated to B'. The angle α is the angle measured by the displacement gage. The angle ρ is the angle measured by the hydraulic actuator RVDT.

3.2.1. Pressure and stroke

Data for load path 1 are shown in Figure 12. The relaxation of axial load at about 125 s, coincided with the internal pressure required to cause yielding under hoop stresses. Similar relaxation of load or torque caused by yielding during a subsequent step is present throughout the validation test data. About two-thirds of the way through step 2, a pressure jump occurred. Smaller pressure jumps were recorded during other experiments, but the cause was not determined. During step 3, the diametric displacement gage went out of range. Similar issues with the diametric displacement measurements persisted throughout the experiments. Fortunately, the diametric changes are only one data set for comparison between model predictions and experimental results. Figure 13 shows the load path 1 specimen after testing.

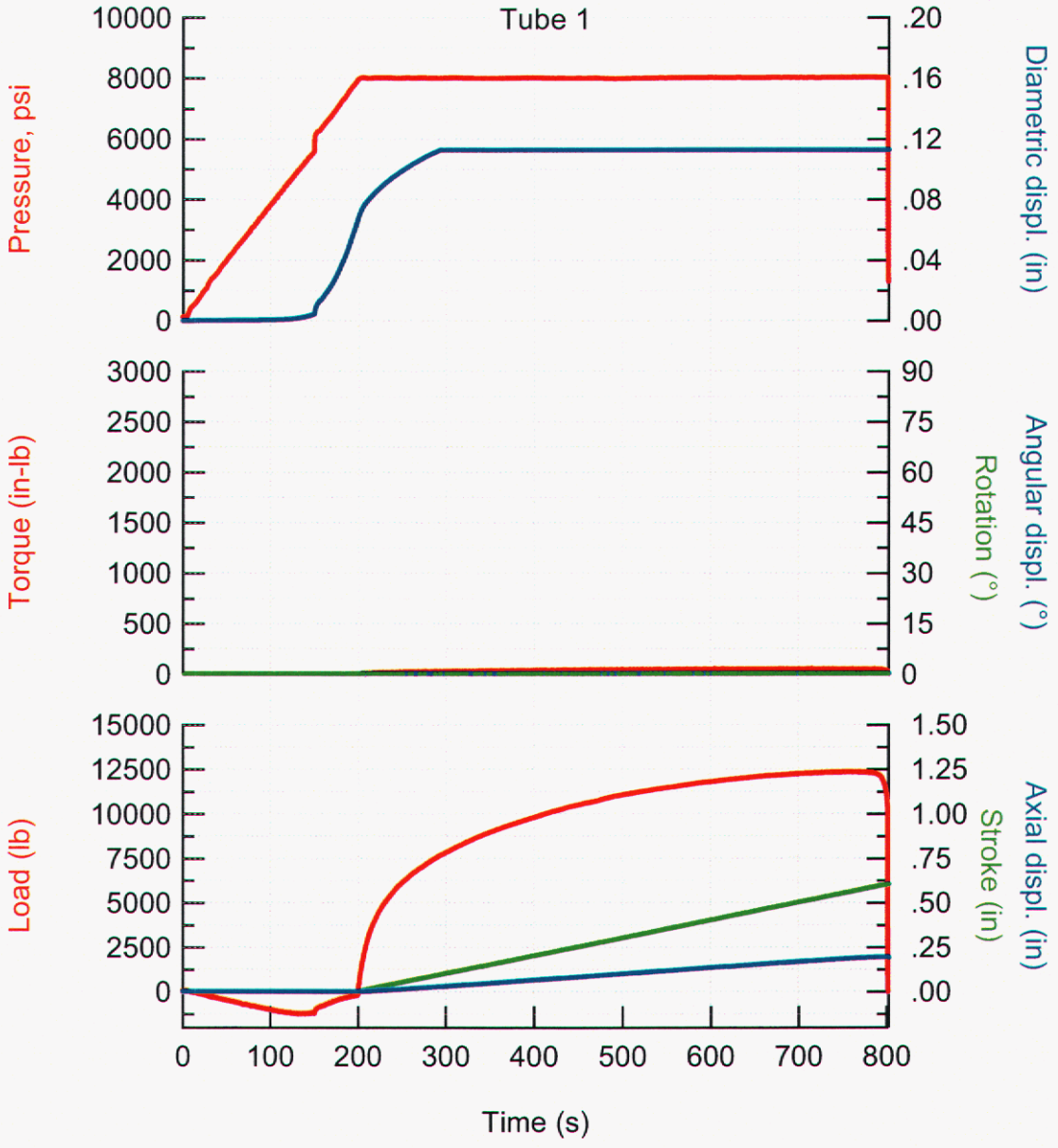

Figure 12. Load path 1 data.

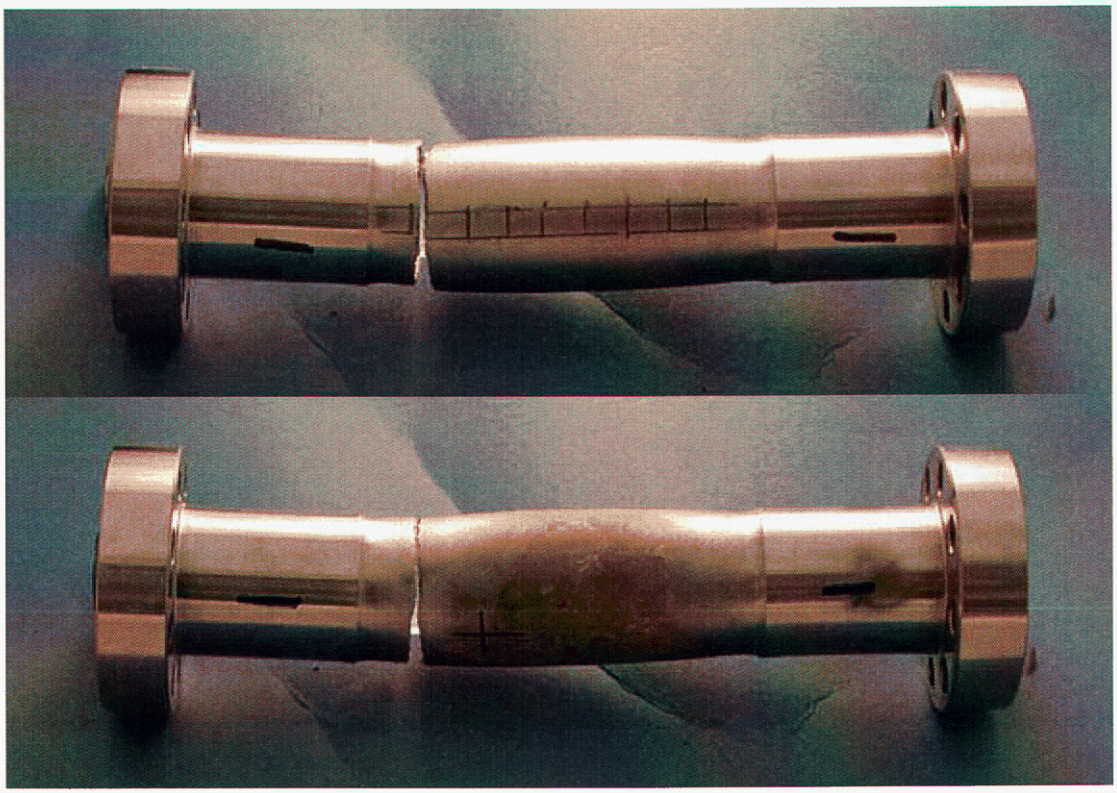

Figure 13. Load path 1 specimen after testing.

Data for load path 2 are shown in Figure 14. Because the internal pressure was not sufficient to cause yielding, the axial load increased in compression until step 3, stroke to failure. The diametric displacement gage went out of range at the end of step 3. Figure 15 shows the load path 2 specimen (tube 2) after testing.

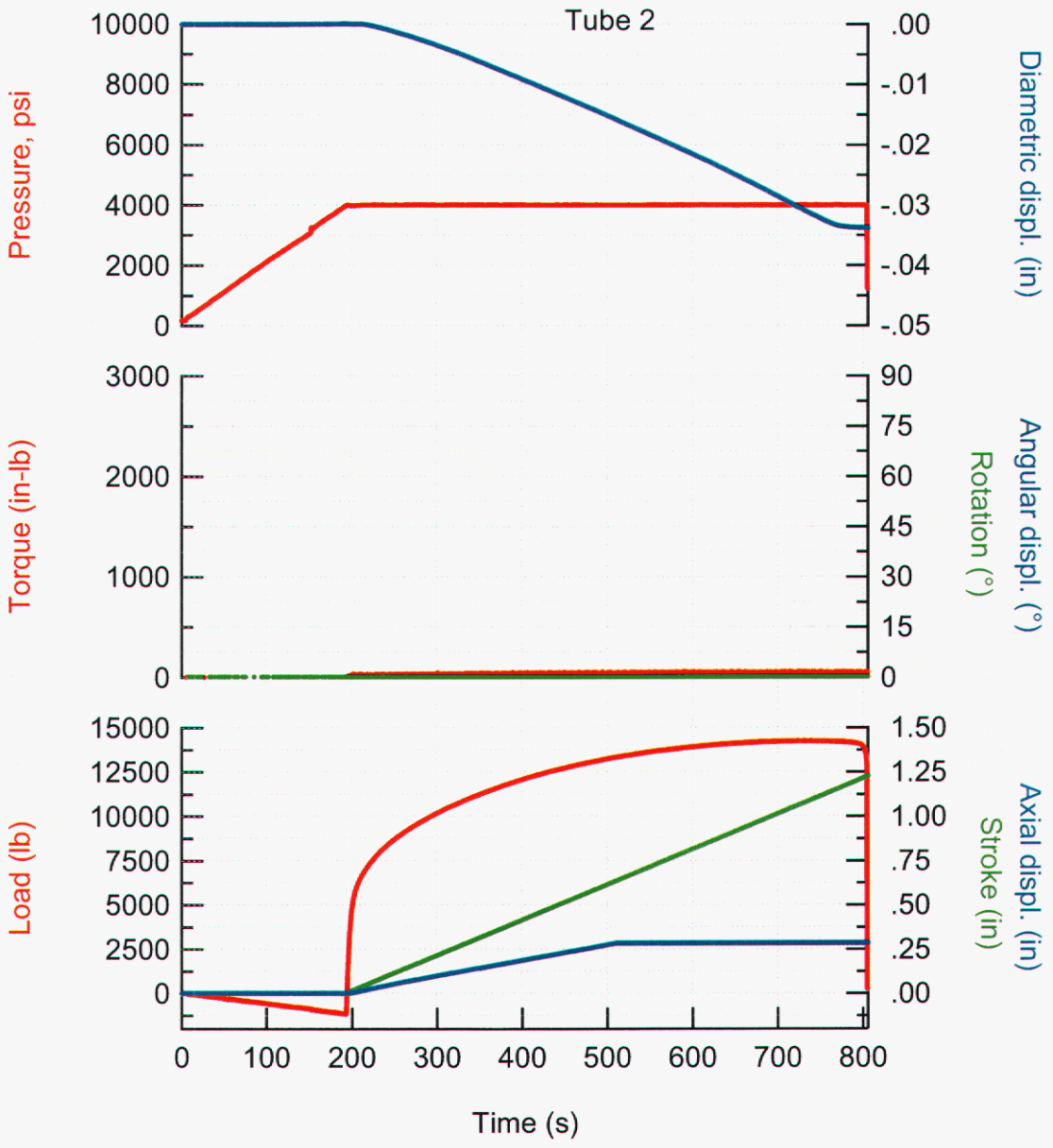

Figure 14. Load path 2 data.

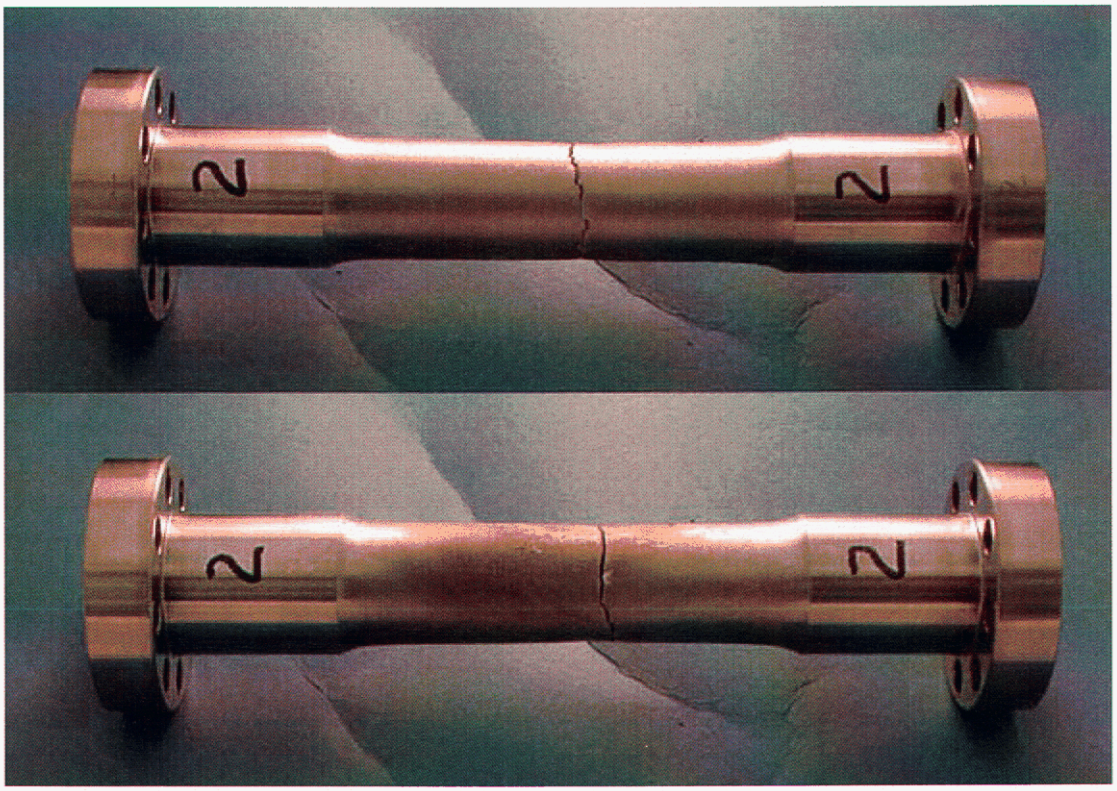

Figure 15. Load path 2 specimen after testing.

3.2.2. Pressure, stroke, and rotation

Load paths 3 and 4 were intended to cause failure during rotation. However, because of the large ductility of 304L, the rotational actuator reached its maximum travel before the onset of failure. The specimens were removed from the test frame, the rotational actuator reset, and the experiment was continued. The unloading portion of the experiment was accomplished manually, and the data was not recorded. Prior to the second and third loadings, pressure was ramped to the level at the end of the first loading. Because the axial force had relaxed to zero by the end of the first loading, axial displacement was not included in the second and third loadings. During the pressure step of the second and third loadings, the axial load should have been controlled at 0 lb, then stroke control resumed for the third step. Fortunately, the axial load developed from internal pressure was small, and holding in axial stroke control may simplify the boundary conditions for modeling the second and third loadings. At the end of the third loading, the specimens showed significant buckling and the experiments were ended. Figure 16 shows the data from all three loadings for load path 3. The Figure 17 contains images of the specimen after testing. Figure 18 shows data for load path 4. Figure 19 contains images of the load path 4 specimen after testing.

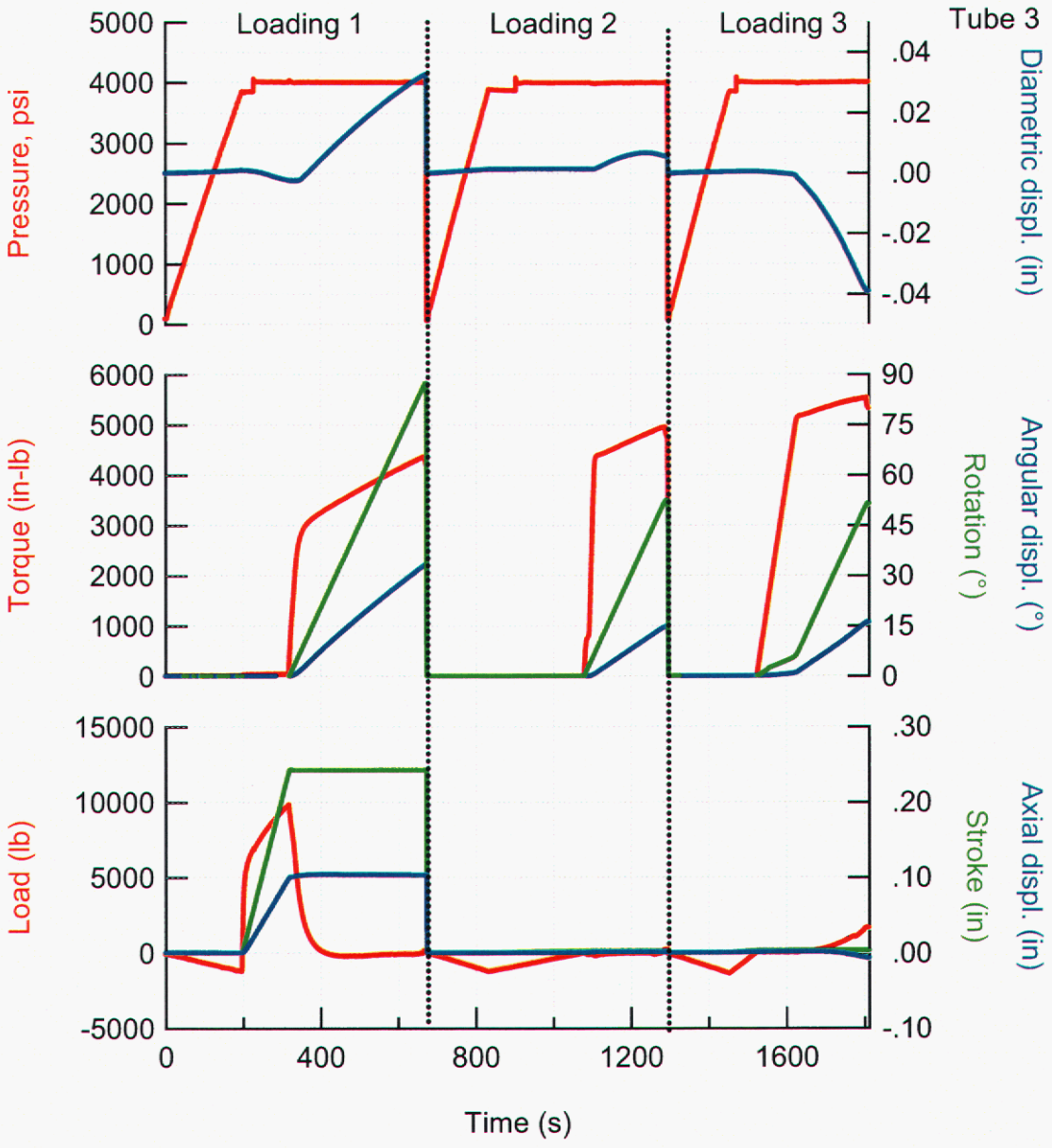

Figure 16. Load path 3 data.

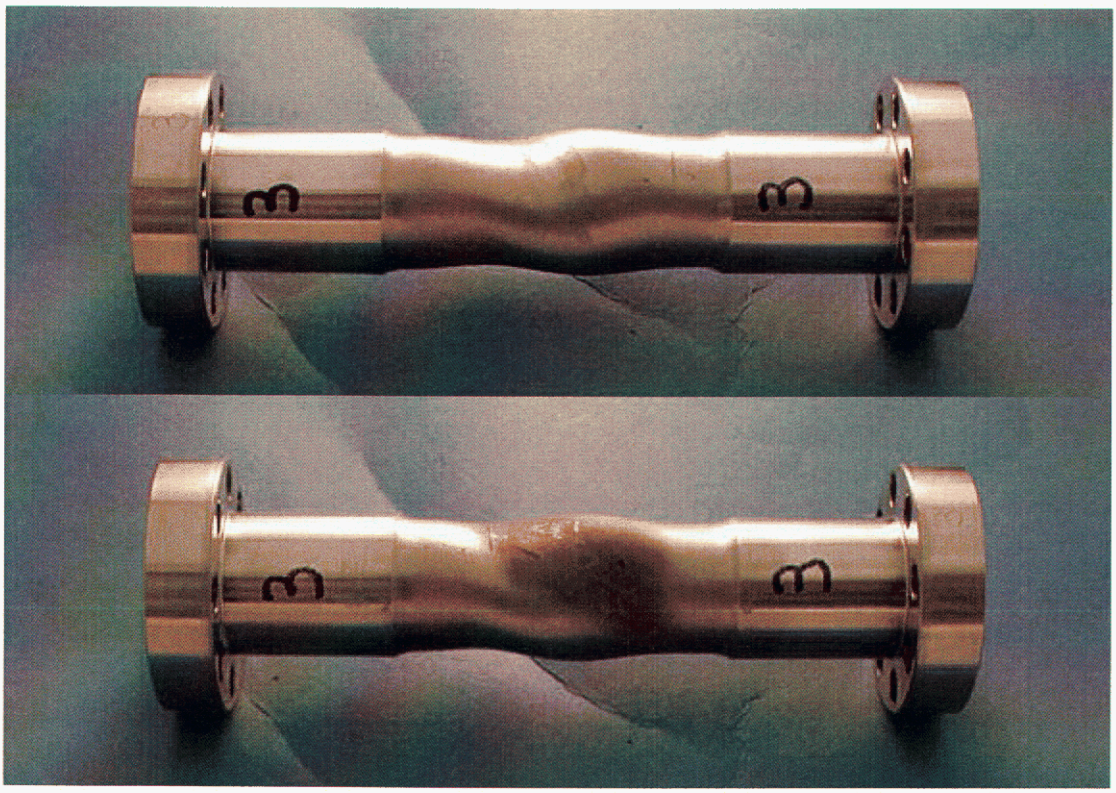

Figure 17. Load path 3 specimen after three loadings.

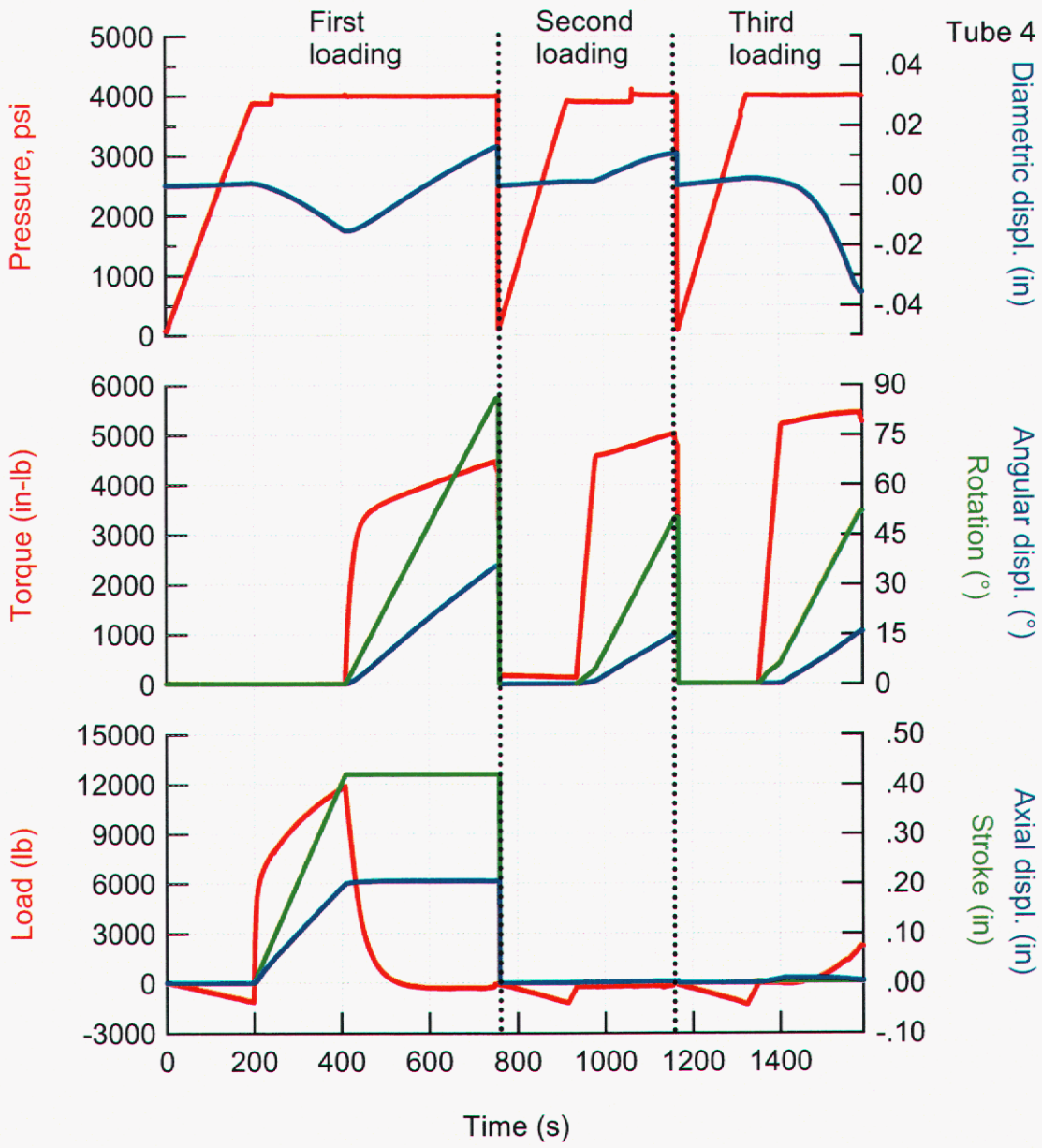

Figure 18. Load path 4 data.

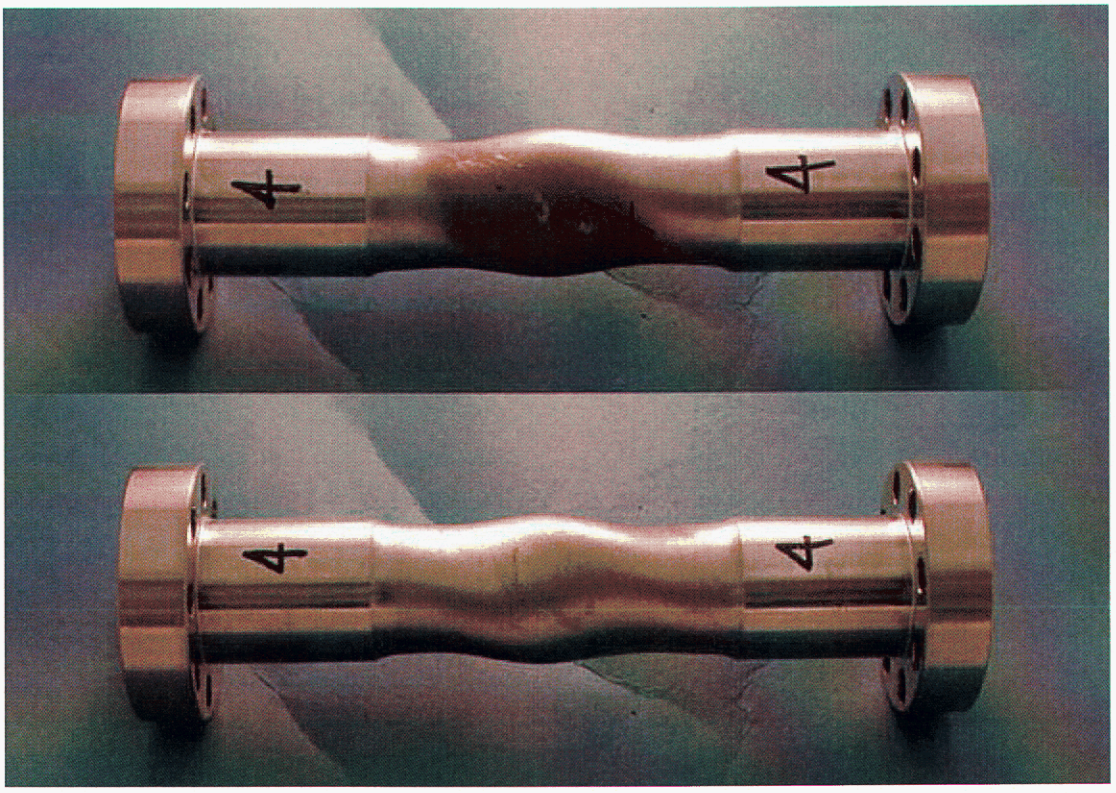

Figure 19. Load path 4 specimen after testing.

3.2.3. Rotation and stroke

Data for load path 5 is shown in Figure 20. The diametric displacement gage went out of range after step 3. Adjustments were made to the displacement gage rods to reduce the risk of the LVDT's going out of range during subsequent experiments. During step 3, the axial displacement gage slipped. The dotted blue line extending the axial displacement curve in Figure 20 was taken from the stroke data. Because the axial load was not changing much during that segment of the test, the changes in stroke and axial displacement would have been very close to the same value. The Load path 5 specimen after testing is shown in Figure 21.

Data for load path 6 is shown in Figure 22. In this case, some of the diametric expansion during rotation was out of range, but the majority of the contraction during the stroke step was recorded. Near the axial peak load, the diametric change slowed down, a result that was attributed to the location of the measurement. Since the diametric LVDT's were located above the location of final minimum diameter, the rate of diameter change during non-uniform deformation would slow down from the rate during uniform deformation. The deformed load path 6 specimen is shown in Figure 23. Data for load path 7 are shown in Figure 24 and images of the deformed specimen are shown in Figure 25. Comments regarding load path 7 data are the same as for load path 6.

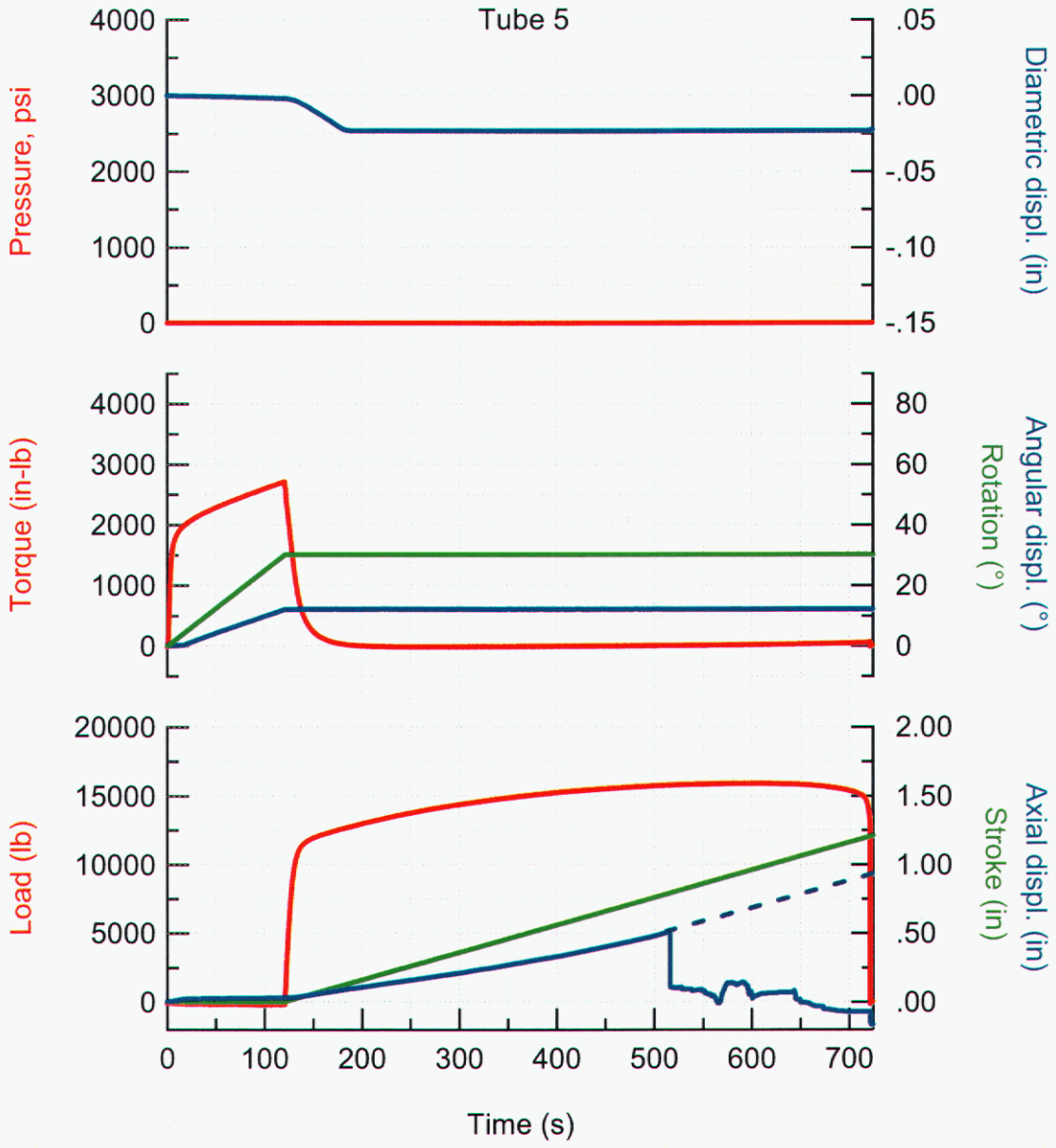

Figure 20. Load path 5 data.

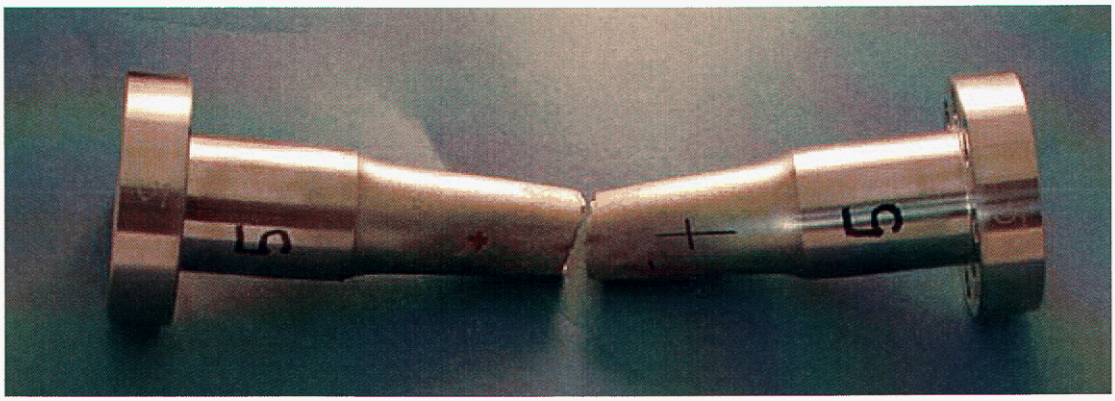

Figure 21. Load path 5 specimen after testing.

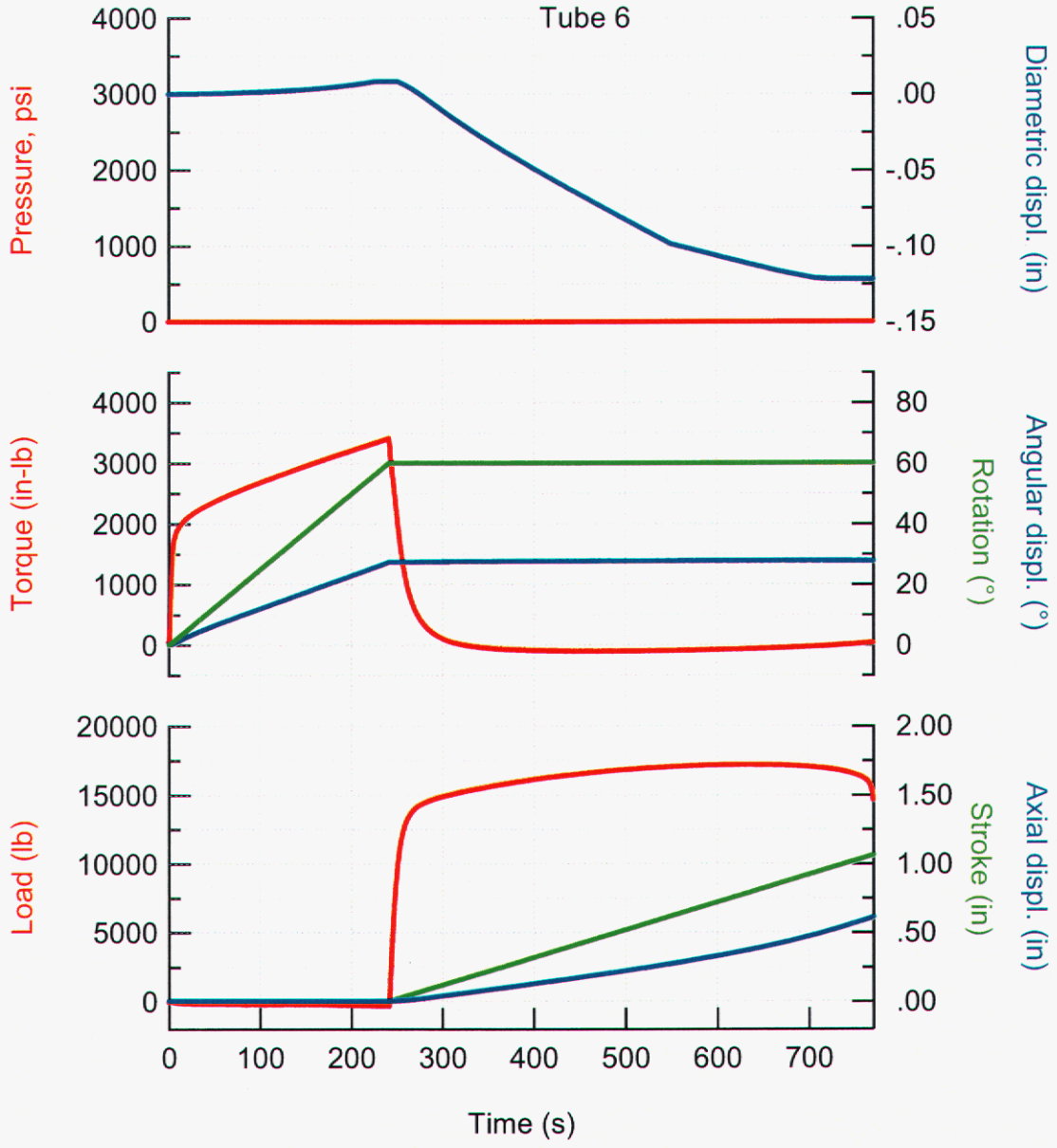

Figure 22. Load path 6 data.

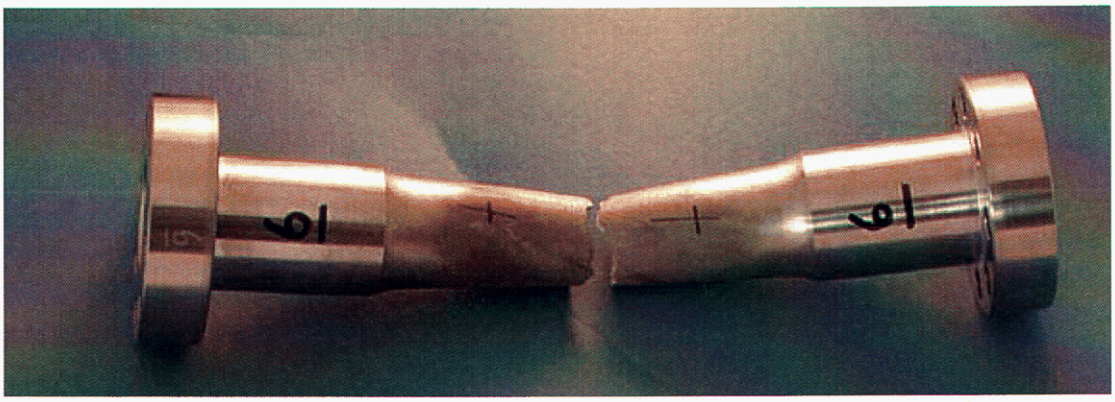

Figure 23. Load path 6 specimen after testing.

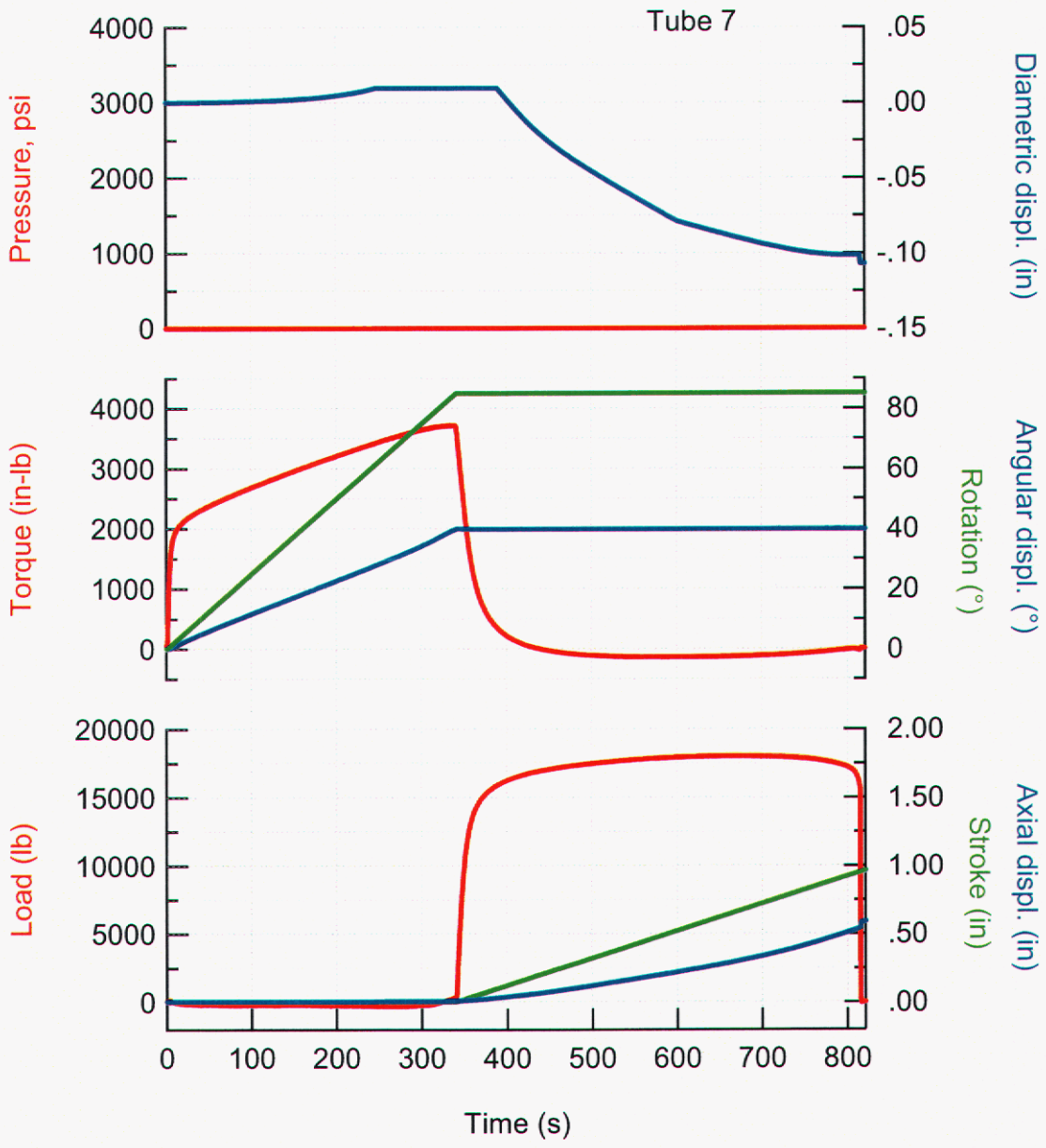

Figure 24. Load path 7 data.

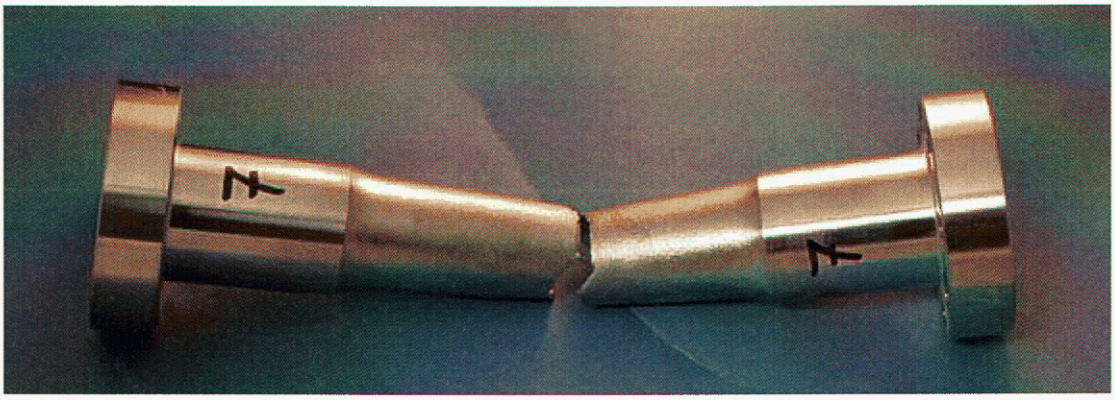

Figure 25. Load path 7 specimen after testing.

3.2.4. Pressure, rotation, and stroke

The data for load paths 8 through 12 contained all of the features that have been commented on regarding the other load paths. The data and images of deformed specimens are shown in Figure 26 through Figure 34.

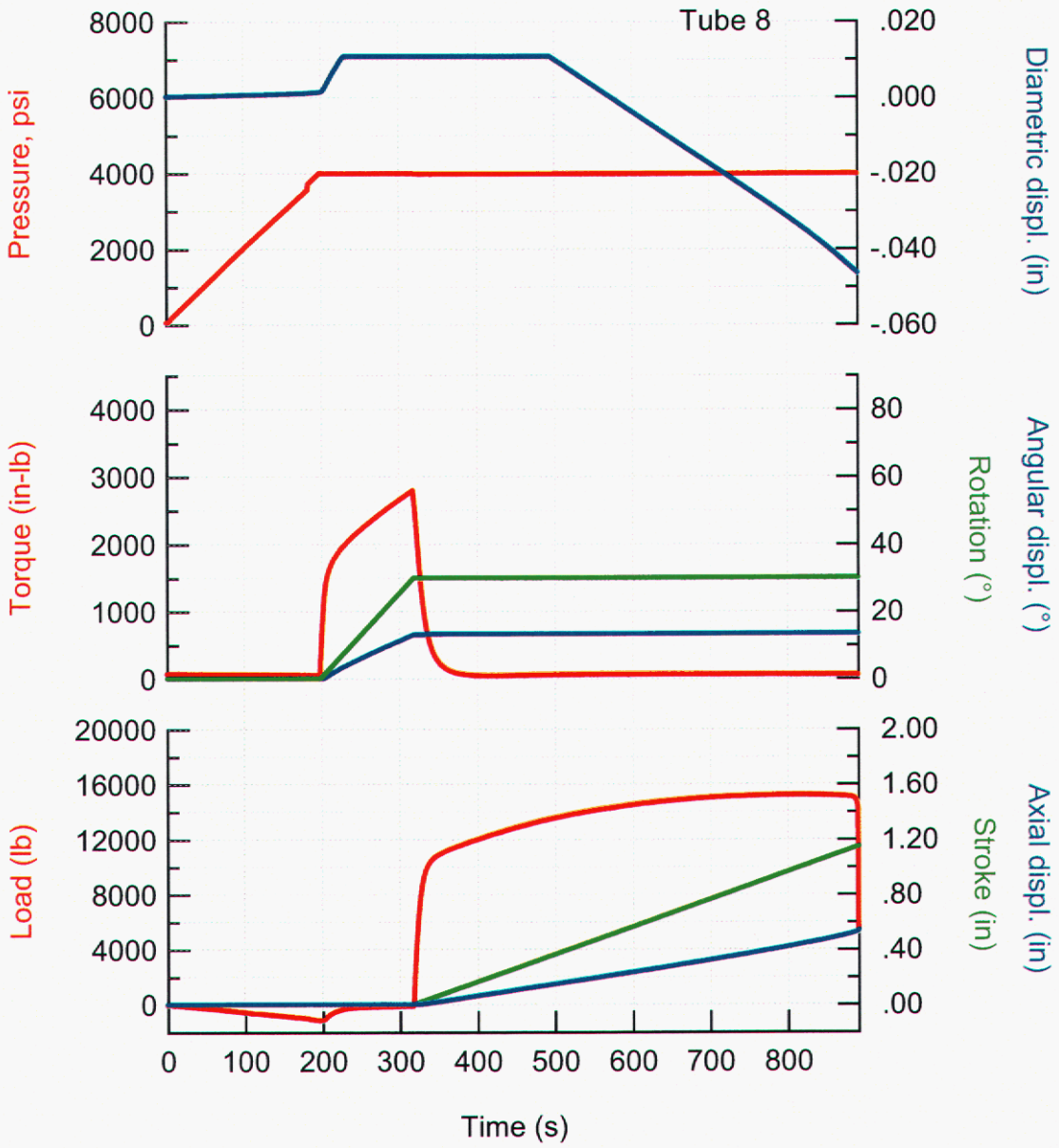

Figure 26. Load path 8 data.

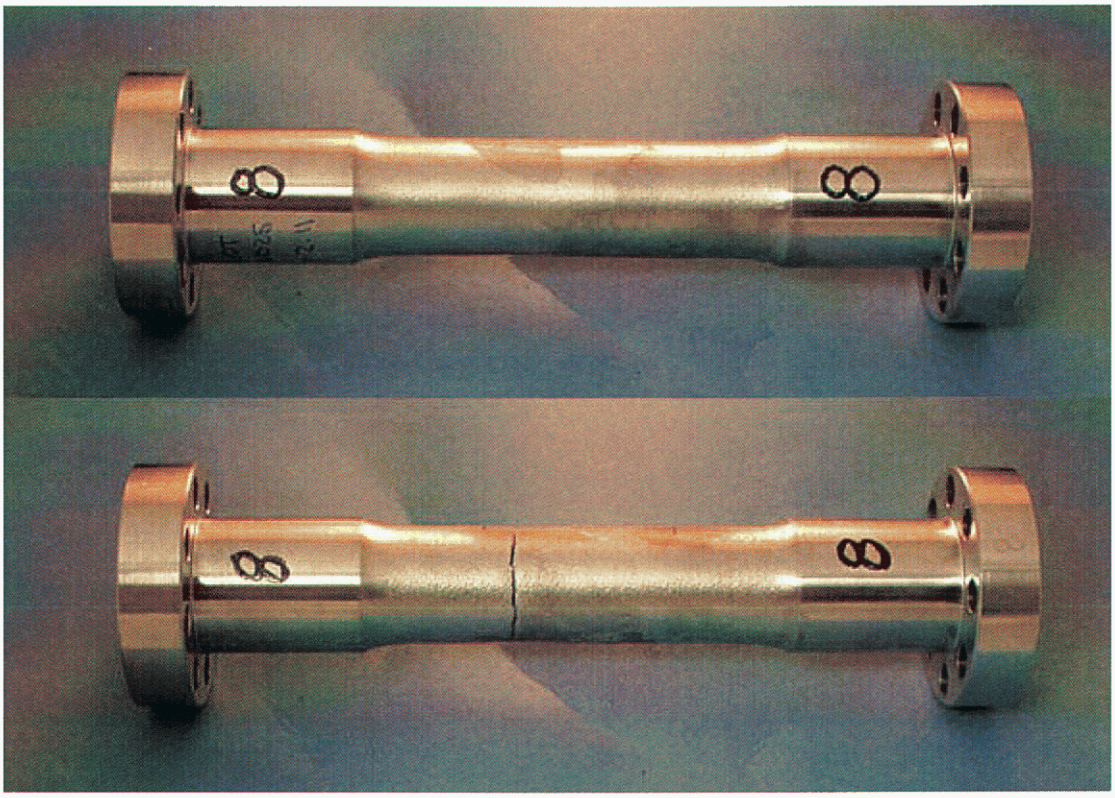

Figure 27. Load path 8 specimen after testing.

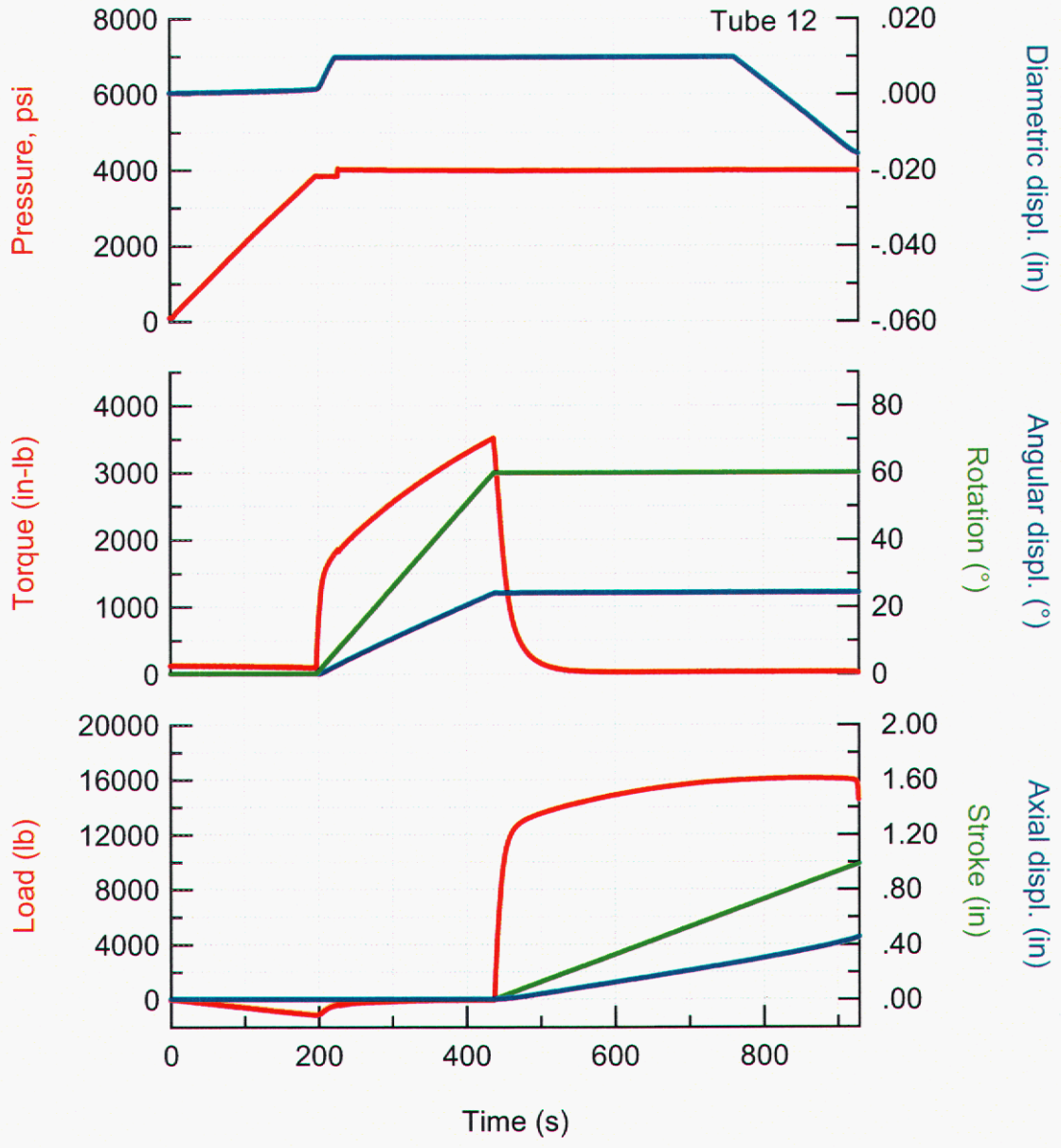

Figure 28. Load path 9 data.

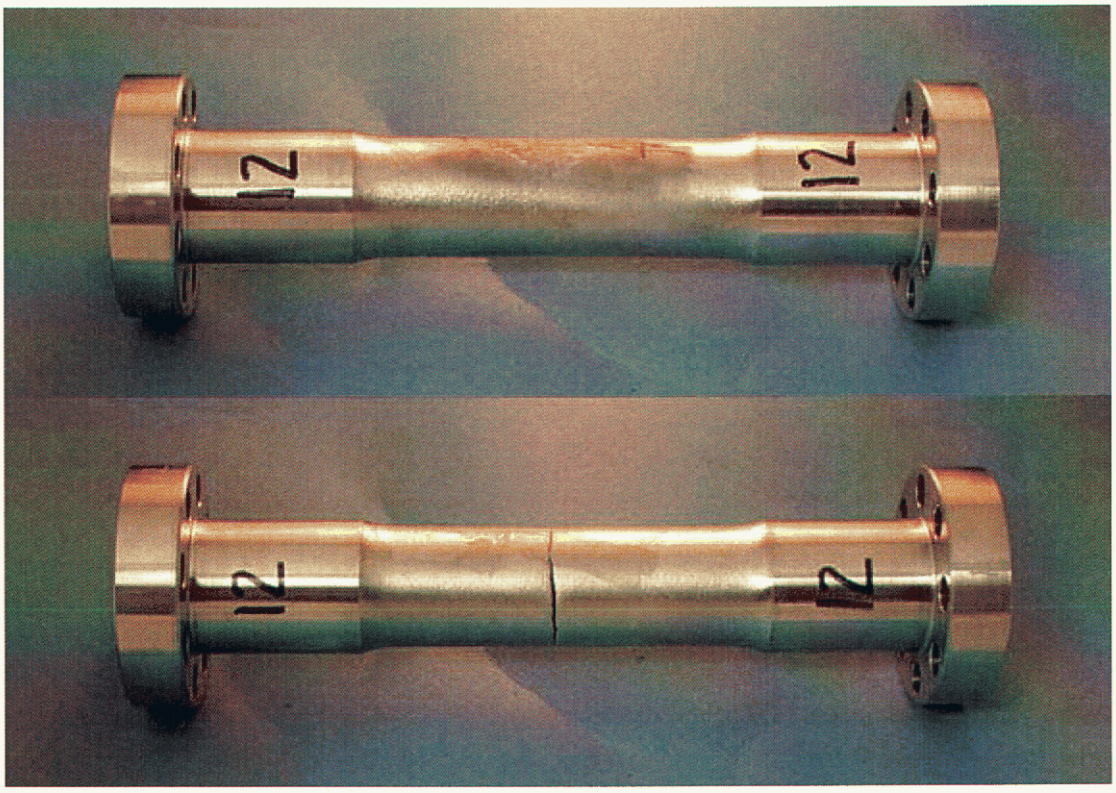

Figure 29. Load path 9 specimen after testing.

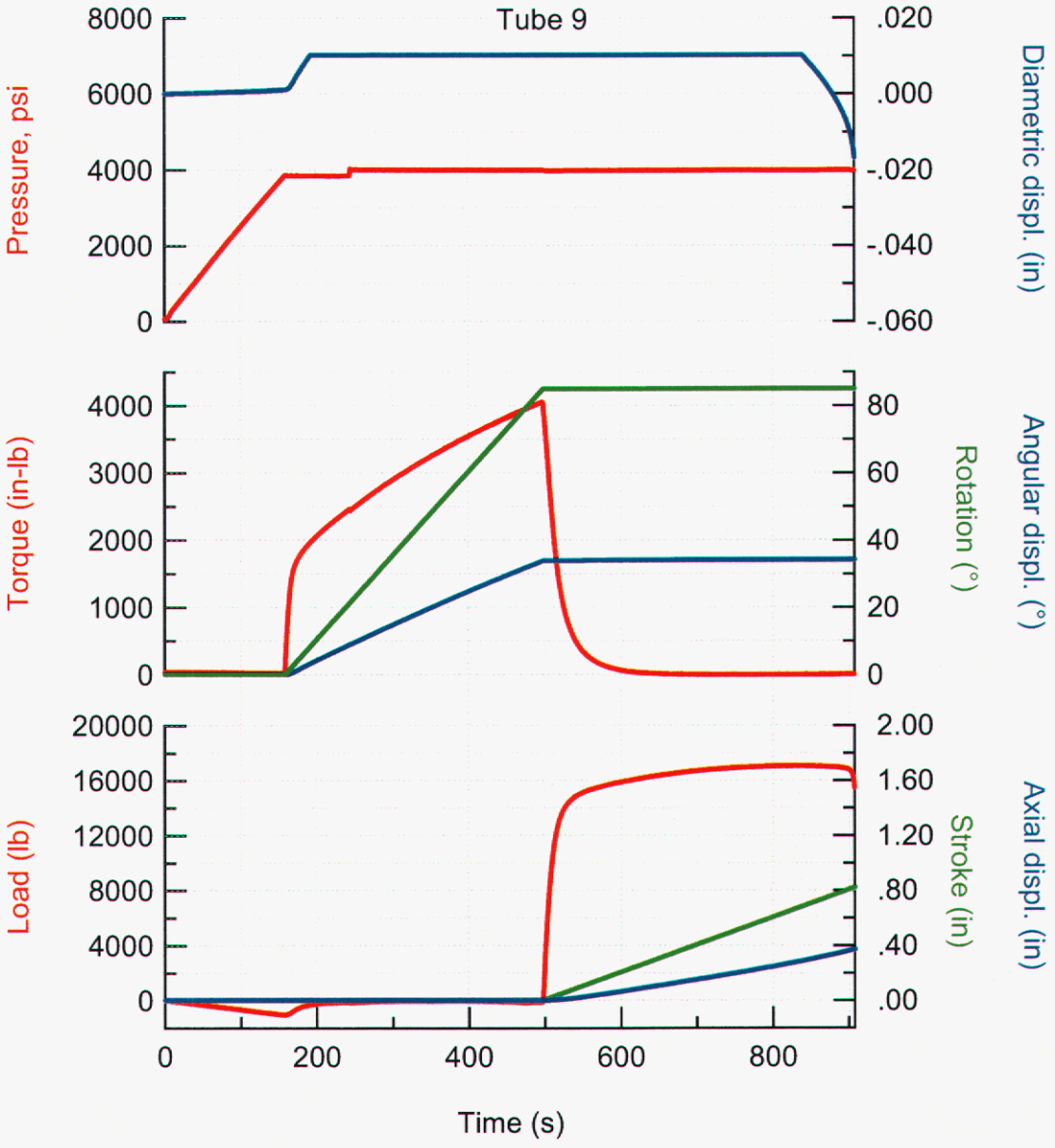

Figure 30. Load path 10 data.

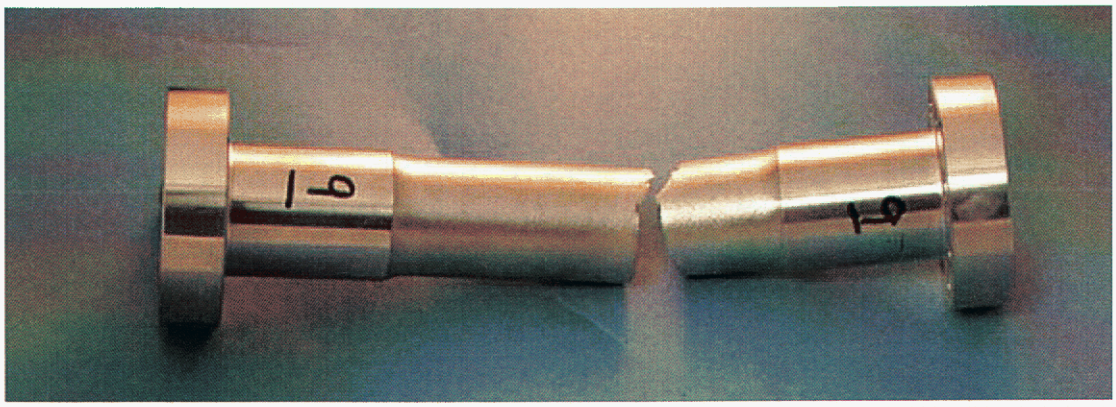

Figure 31. Load path 10 specimen after testing.

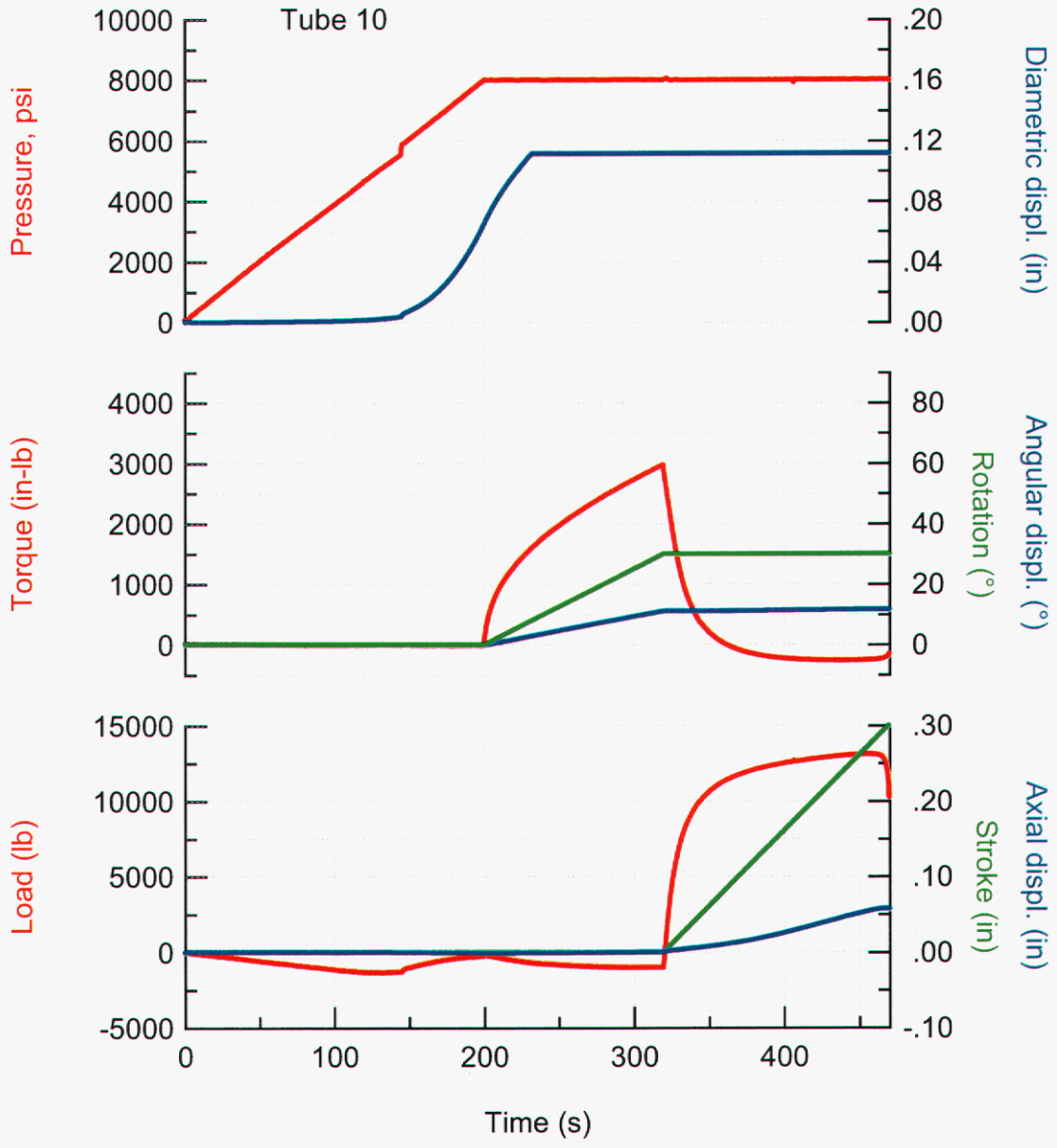

Figure 32. Load path 11 data.

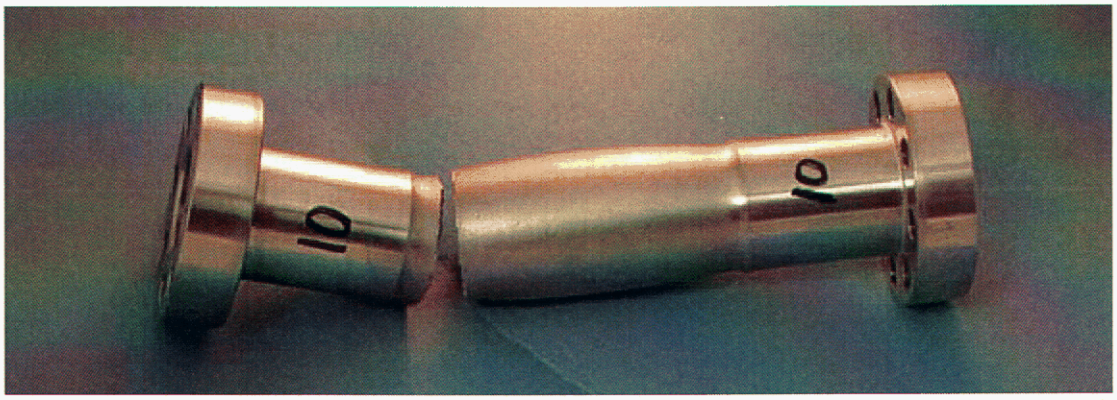

Figure 33. Load path 11 specimen after testing.

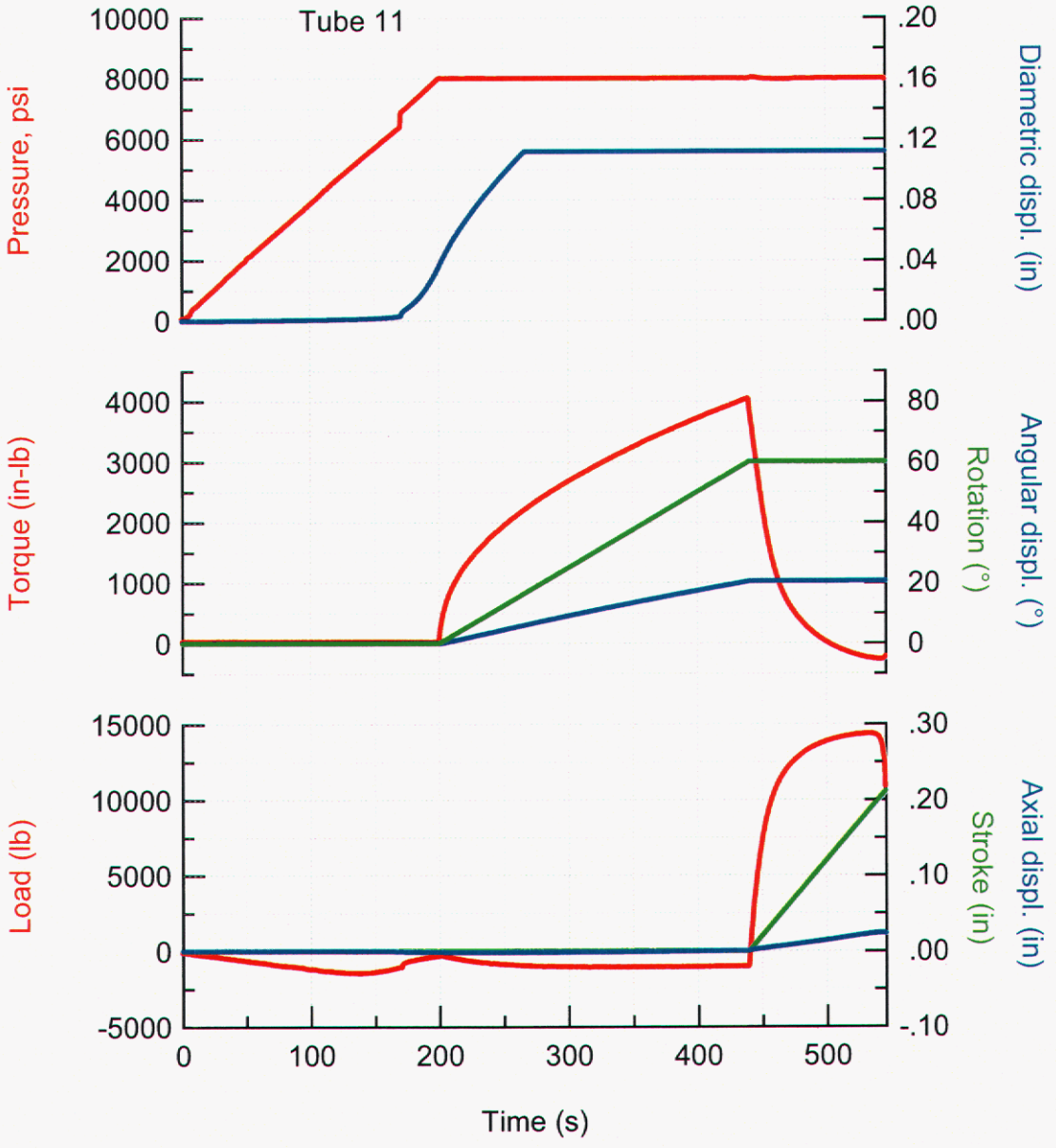

Figure 34. Load path 12 data.

Figure 35. Load path 12 specimen after testing.

3.2.5. Machine compliance

Machine compliance was measured for axial and torsional loading of the test frame using the solid steel specimen described in the section on experimental details. Figure 36 shows the axial compliance data and the calculated compliance correction curve, which is the displacement difference between the stroke measurement and the calculated elastic displacement of the solid steel link. A linear fit of the axial compliance correction curve had a slope of 6.92 in/lb. A second-order polynomial fit of the compliance correction curve with the form Y=K0+K1(load)+K2(load)^2), had coefficients: K0=8.886e-5, K1=4.972e-7, and K2=1.053e-11.

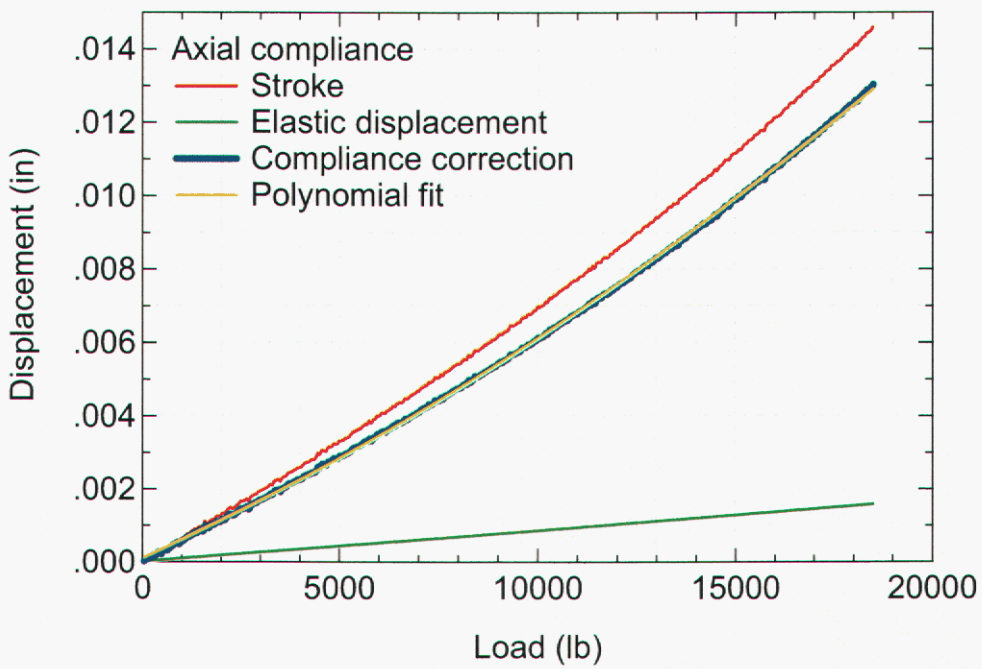

Figure 36. Axial compliance data.

Torsional compliance data is shown in Figure 37. A linear estimate of the compliance correction curve had a slope of 3.452e-5 degrees/in-lb. A second-order polynomial fit of the compliance correction curve, with the form Y=K0+K1(torque)+K2(torque)^2), had coefficients: K0=9.130e-4, K1=2.967e-5, and K2=8.021e-10.

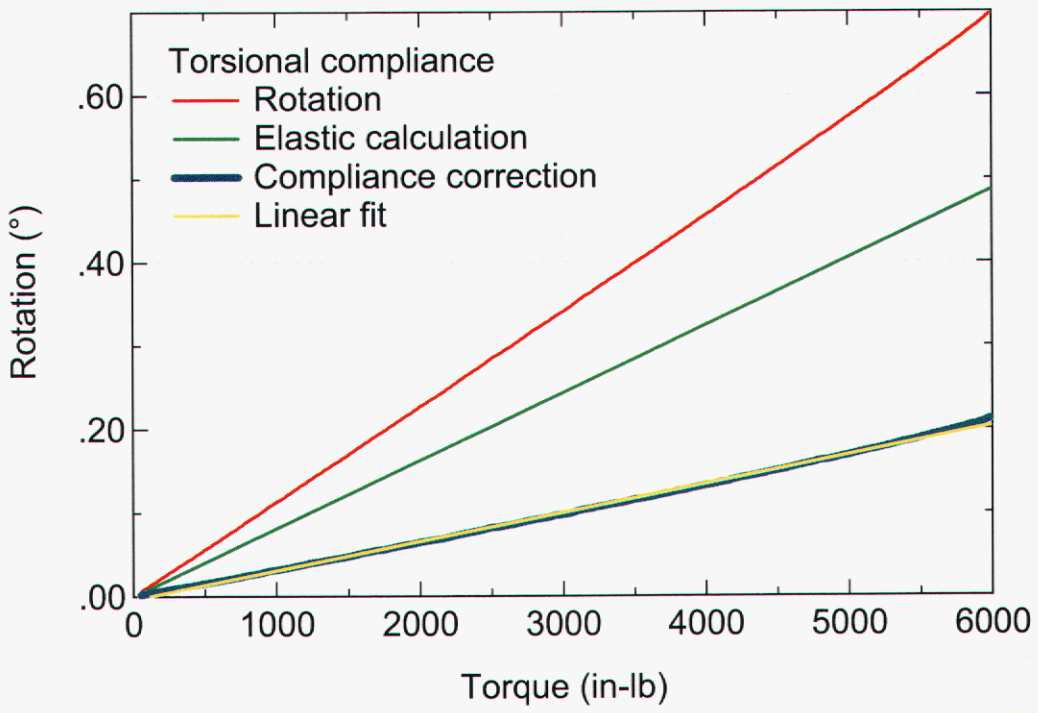

Figure 37. Torsional compliance data.

4. Comments

The validation experiments did not reveal surprising results. The interactions between loading paths can be understood through established concepts of mechanical behavior. The value of this effort lies in providing experimental data for comparison to material model simulations of path dependent plasticity and failure.

Generally, it is good practice to perform replicate experiments for any given set of conditions. In this case, replicates of individual validation experiment loading paths were not completed, primarily due to cost and time constraints. However, there are many similar conditions between the different loading paths which can be used to increase the confidence that significant differences in behavior would not be revealed through replicate experiments. In addition, the calibration test data show levels of variation that suggest little would be gained by conducting replicate tests. If additional experiments were determined to be of use, the experimental set up is present and functional.

In the event that additional combined loading experiments were to be performed, a few refinements to the setup should be made. The diametric displacement gages should be modified to cover the full range of specimen diameter change. The pressure system should be evaluated in an effort to eliminate pressure jumps. This is a control issue that might be resolved by tuning, or pressure sensor selection. The range of the torsional actuator is a basic limitation. If reloading experiments were to be continued, best practice would be to control and record the unloading segments. The use of a different axial torsional load frame with a larger range of rotation might be an option. A 50 kip frame is available in this department that has a 10-turn range, but control issues would have to be resolved prior to performing the experiments.

This page intentionally left blank.

5. References

1. Materials Weapon Information System and Data Management application, http://www-irn.sandia.gov/wisdm/ , Catalog:\Metals\Stainless Steels\Steel, Stainless 304L\Annealed\Test Suite: WR 4 in diam bar from FM&T.

2. Han-Chin Wu, Zhiyou Xu, An Axial-Torsional Extensometer for Finite Deformation, Journal of Engineering Materials and Technology Transactions of the ASME, pp 330-335, vol. 112, 1990.

This page intentionally left blank.

Appendix A
Material certification

QUALITY ACCEPTANCE CERTIFICATION REPORT	Allied Signal Aerospace P.O. Box 419159 Kansas City, MO 64141-6159	Material Control Number 200357 1 thru 5 Date:

SAMPLE HISTORY	CARPENTER TECHNOLOGY CORP.
Quantity Received:	Applicable Specifications: Applicable Drawings: 9851810
PO Number:	B514949-013-002
Size:	4"(+/-.005) X 12' Diameter
Heat No.:	517190
Alloy Type:	304L S.S.

TEST RESULTS

I. Physical and Mechanical Properties

	Strength in KSI				
Alloy & Condition	Yield .2% Offset	Ultimate	Elongation	Reduction in Area	Other
	39.6 & 33.1	82.0 & 80.5	47.3 & 66.5		

II. Metallurgical

Grain Flow:	
Inclusion Rating:	1/2 D THIN, 1 B THIN, 1 D THIN
Grain Size:	80% 3.5 20% 7.0
Delta Ferrite:	<.5%
Hardness:	
Other:	

III. Chemical Analysis (%)

Al	B	C	Co	Cr	Cu	Fe	Mo	Mn	N
0.006		0.024	0.089	18.28		BAL	1.62	0.21	0.05
Ni	**O**	**P**	**S**	**Se**	**Si**	**Ti**	**V**		
11.02	0.002	0.023	0.0030		0.61	<.003			

IV. Nondestructive Testing

Ultrasonic Inspection:
Accepted.

Comments
NB = 0.019%.

Disposition
ACCEPT

Certified By: (08458)
Approved By: MILLER(08458) 07/17/1998
Updated By: MILLER(08458) 10/02/1998

Distribution list

1	MS 0372	J. T. Ostien, 01524
1	MS 0372	J. Pott, 01524
1	MS 0372	G. W. Wellman, 1525
1	MS0372	W.M. Scherzinger, 1524
1	MS 0824	T.Y. Chu, 01500
1	MS 9042	B.R. Antoun, 8776
1	MS 9042	D. J. Bammann, 8776
1	MS 9042	E. P. Chen, 8776
1	MS 9042	M. L. Chiesa, 8774
1	MS 9042	J. J. Dike, 8774
1	MS 9409	J. S. Korellis, 8776
1	MS 9409	S.X. McFadden, 8776
1	MS 9721	K. L. Lee, 8758
2	MS9018	Central Technical Files, 8944
2	MS0899	Technical Library, 4536